Maximizing Vortex Induce Vibrations Through Geometry Variation

Project #: BJSFO11

A Major Qualifying Project Report

Submitted to:

Primary WPI Advisor: Brian James Savilonis

in partial fulfillment for the requirements for the

Degree of Bachelor of Science

Submitted by:

_____

Ian Ball

_____

Thomas Killen

_____

Shubham Sakhuja

_____

Ethan Warner

_____

Professor Brian Savilonis
Primary Project Advisor
Date: April 26th, 2012

Abstract

Large hydro-power extraction systems such as hydroelectric dams can be very expensive to construct and maintain, and have negatives impacts on the environment. An alternative, less intrusive hydro-power extraction system extraction based on the vortex-induced vibration phenomenon is a viable solution to the problem. Vortex induced vibrations are motions induced on bodies as a result of periodic irregularities in the downstream flow separation. Normally, vortex induced vibrations are sought to be eliminated in order to prevent mechanical failure. This project seeks to maximize vortex induced vibrations to efficiently convert flow energy into mechanical energy. A power generation system based on vortex-induced vibrations requires relatively little infrastructure. This allows the system to be placed in areas of low-velocity flow such as rivers and tidal streams.

Table of Contents

List of Figures

List of Tables

Executive Summary

Large hydro-power extraction systems such as hydroelectric dams can be very expensive to construct and maintain, and have negatives impacts on the environment. An alternative, less intrusive hydro-power extraction system extraction based on the vortex-induced vibration phenomenon is a viable solution to the problem. Vortex induced vibrations are motions induced on bodies as a result of periodic irregularities in the downstream flow separation. Normally, vortex induced vibrations are sought to be eliminated in order to prevent mechanical failure. Our project seeks to maximize vortex induced vibrations to efficiently convert flow energy into mechanical energy.

To maximize power output, the system must operate at a condition known as “lock in”. Lock-in occurs when the frequency of vortices forming behind the bluff body approach the natural frequency of the system to which it is attached. This system resonance results in large oscillation amplitudes. The power generated by an object driven by vortex induced vibrations is a function of oscillation amplitude and frequency. The goal of this project was to explore different shedder geometries that could provide a greater energy conversion rate (power output) than a cylinder.

Using the Flow Simulation package in SolidWorks, we performed computational fluid dynamic (CFD) analyses on a cylinder and various T-shapes at a range of Reynolds numbers to determine expected oscillation amplitude and oscillation frequency. From the computational fluid dynamics results, lift coefficients (as a measure of normalized shedding force) and Strouhal numbers (normalized shedding frequency) were determined for each of the geometries tested. These results revealed the geometry with the highest power coefficient, a low aspect ratio T-shape.

To compare these CFD results to physical experiments, a flow test facility was constructed to provide an environment in which to test the various geometries. A constant-level head tank was combined with a recirculating pump system to create a steady, uniform flow. The geometries under test were mounted to a pivoting beam oscillator that was designed to have an adjustable natural frequency. A custom designed, optical point tracking data acquisition system was developed to provide real-time oscillation data feedback. Shedder position data was captured as the oscillator natural frequency was adjusted incrementally. The experimental shedder position data was analyzed using a Fast Fourier Transform to provide a dimensionless amplitude and a dominate frequency. The results confirm agreement between oscillation theory, computational fluid dynamics, and experiment, showing that the lock-in condition occurs at a specific resonant frequency and does result in the greatest power output.

1. Introduction

For centuries, man has captured energy from moving water. From the first water wheels that drove the mills and mines of ancient times, to the tremendous hydroelectric dams that are used today, moving water has always been seen as a renewable source of power. Unfortunately, all of these devices have one thing in common. A large infrastructure is required in order to direct the flow of water through the device. In the case of hydroelectric dams, this means thousands of tons of concrete behind which hundreds of acres of land are submerged under reservoirs. Needless to say, these changes to the landscape can have a tremendous impact on the natural ecosystems not only in the area of the dam, but also miles up and downstream.

In order to make hydroelectric power generation not only pollution-free but also environmentally friendly, a new kind of power extraction system needs to be developed. A hydro-power extraction system based on the vortex-induced vibration phenomenon can be a viable solution to the problem. Vortex induced vibrations are motions induced on bodies as a result of periodic irregularities in the downstream flow separation. Normally, vortex induced vibrations are sought to be eliminated in order to prevent mechanical failure of the vibrating structures. Instead of minimizing these vibrations, for this application they are sought to be maximized for increased energy capture.

A system based on VIV has several distinct advantages. First, they require relatively low flow velocities for operation, which eliminates the need for dams or channels to increase the water velocity. This also allows the system to be placed in areas of natural low-velocity water flows such as small rivers and tidal streams. A recent study by Georgia Tech Research Corporation showed that the average tidal stream power density in some areas is as high as 8 kW/m^2 with surface areas on the order of few hundred kilometers squared. [23]

Endangerment to wildlife is also a major concern with complex hydropower systems. In a typical hydro turbine, known as a Kaplan turbine, many dangerous flow conditions encountered during passage through the turbine pose a threat to fish [22]. Some of these dangers include strike, shear, grinding, turbulence, cavitation, pressure changes, and even high dissolved gas levels. The oscillation components of VIV systems move at a relatively slow velocity, and allow open passage or avoidance of the system completely, which reduces the risk of harm to wildlife in the immediate vicinity of the device.

In order to further the development of a power extraction system based on VIV, extensive research was done to determine a more efficient shape for the shedder (the vibrating structure) in terms of power extraction than a simple cylinder. A two-pronged approach was taken which analyzed a series of geometries with computational fluid dynamics, as well as experimental testing to confirm the results in a real-world flow environment.

2. Background

2.1 Vortex Induced Vibration

Vortex induced vibrations are a result of vortex shedding phenomenon. Vortices can be produced when a bluff body is placed within a fluid flow [1]. As the fluid flows around the bluff body, a boundary layer forms. Depending on the flow characteristics and geometry of the body, boundary layer separation occurs. Since the outside edge of the separated boundary layer is adjacent to the free stream and moving at a higher velocity than the inside edge of the boundary layer, a shear layer forms and the fluid rotates. The rotating fluid forms vortices that "shed," or separate from the body, in different patterns throughout the wake. When the vortices behind the body are not symmetrical on the top and the bottom, the resulting pressure differential induces lift forces perpendicular to the direction of the fluid flow. The periodic formation of vortices mean the lift forces vary with time and cause oscillating motion of the bluff body.

One flow characteristic that governs the behavior of vortex shedding is the Reynolds number. The Reynolds number is directly related to the flow velocity (U), the characteristic length of the body (L) and the kinematic viscosity of the fluid (ν): shown in equation 1.

$$Re = \frac{U \times L}{\nu} \qquad \textbf{Equation 1}$$

Figure 1 below shows the various vortex shedding regimes and the Reynolds numbers at which they occur.

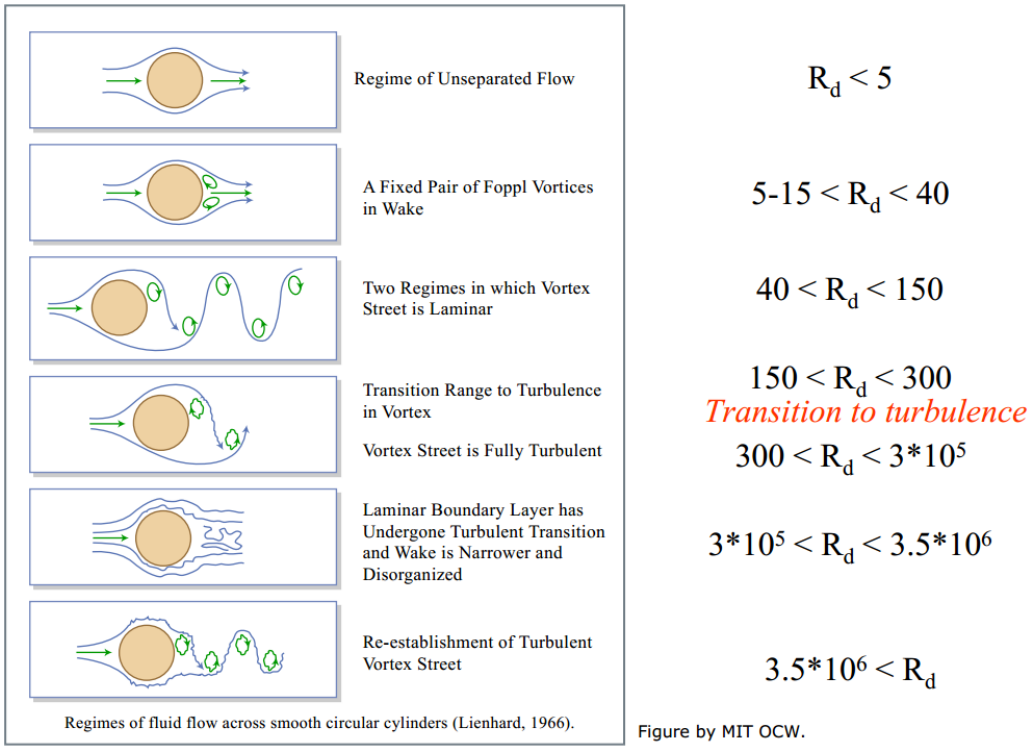

Figure 1: Vortex Shedding at Specified Range of Reynolds Numbers [2]

For the natural low-flows considered for this project, the regime that is targeted is the "Fully Turbulent Vortex Street" regime, with Reynolds numbers in the range of $300 < R_d < 3 \times 10^5$. In addition to the Reynolds number which serves as a non-dimensional ratio of inertial to viscous forces, the Strouhal Number is a non-dimensional parameter that describes the vortex shedding frequency. The Strouhal number is a function of the characteristic length of the body, the vortex shedding frequency, and the flow velocity, and can be seen in equation 2.

$$St = \frac{L \times f_s}{U}$$ **Equation 2**

The Strouhal number varies with Reynolds number for a given shedder geometry as seen in Figure 2 for a cylinder. The discontinuity in the graph is attributed to the range of Reynolds

numbers between $3.0*10^5$ and $3.5*10^6$ where there is a narrow wake and no organized vortex shedding. Reynolds numbers greater than $3.5*10^6$ correspond to the largest Strouhal numbers.

Over the range of Reynolds numbers considered in this project, the Strouhal number is relatively constant at 0.21.

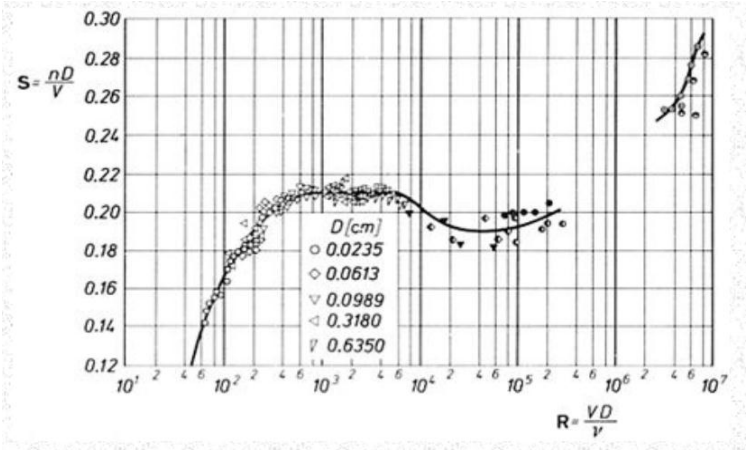

Figure 2 - Strouhal Number vs. Reynolds Number for a cylinder

A phenomenon known as "lock in" [3] has the potential to develop large amplitudes of oscillation. Simply, vibration amplitudes of the cylinder will increase as the shedding frequency approaches the natural frequency of the cylinder. However, lock in does not occur at the exact natural frequency of shedding frequencies because the cylinder oscillations limit the vortex shedding process. As the cylinder oscillations increase in amplitude, vortex shedding is lessened and reduces continued motion. The reduced velocity [4], U^*, is typically used to measure vibration amplitude.

$$U^* = \frac{U}{f_n \times D} \qquad \textbf{Equation 3}$$

Experimental data for lock in has shown that lock in occurs when U^* is between 3 and 8. In addition to U^* lock in depends on another parameter known as the mass ratio:

$$M^* = \frac{M_{osc}}{M_d}$$ **Equation 4**

M_{osc} represents the mass of the oscillator and M_d is the mass of the displaced fluid. Figure 3 below shows the relationship between reduced velocity U^* and mass ratio M^*.

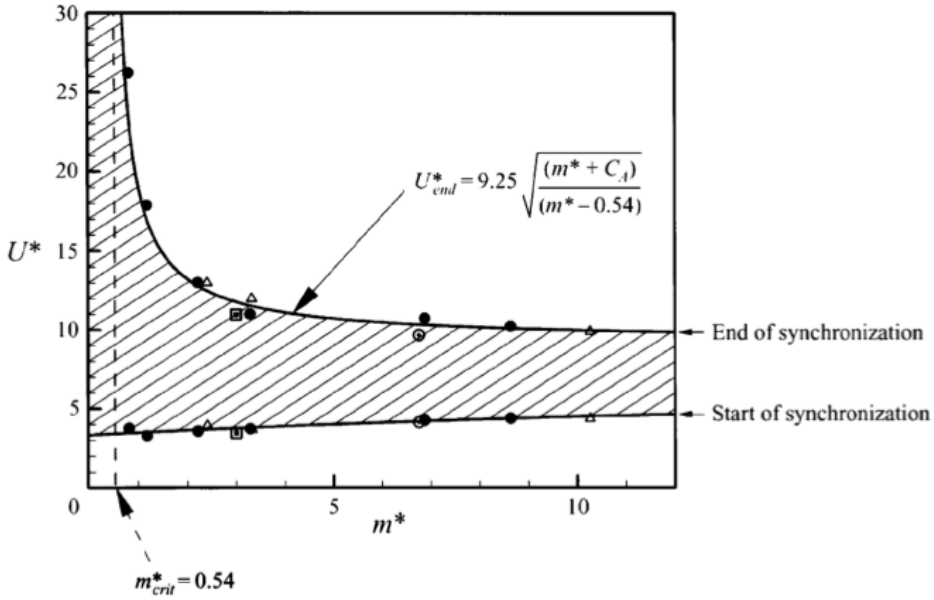

Figure 3 - Reduced Velocity U* Plotted Against Mass Ratio m* [4]

Lock-in occurs when the operating conditions correspond to parameters that intersect within the shaded area.

2.2 Current Applications

There are several practical applications of power generation from vortex-induced vibrations, each in various stages of development. These systems operate on one of several different principles, including oscillating cylinders and vibrating tensioned cables. ["Energy harvesting using vortex-induced vibrations of tensioned cables"]

The closest system to commercial availability is based on using VIV to oscillate cylinders mounted on underwater structures. Vortex Hydro Energy [5], is developing the Vortex Induced

Vibrations Aquatic Clean Energy (VIVACE) converter to harness hydrokinetic energy. The converter harnesses the motions created by vortex induced vibrations on cylindrical shedders from the water current that flows over them.

The device was created at the University of Michigan with the goal of harnessing energy from a low-velocity water current to generate electricity. The flows targeted by the VIVACE system are in the range of 2 to 4 kts (1 to 2 m/s), too slow for typical turbine power generation [5]. The system is comprised of a support frame with an array of cylinders placed at the bottom of a river. The water passes over the cylinders and the vortex induced vibrations cause them to oscillate vertically. The shedders move clusters of magnets through a wire coil to induce an electrical current.

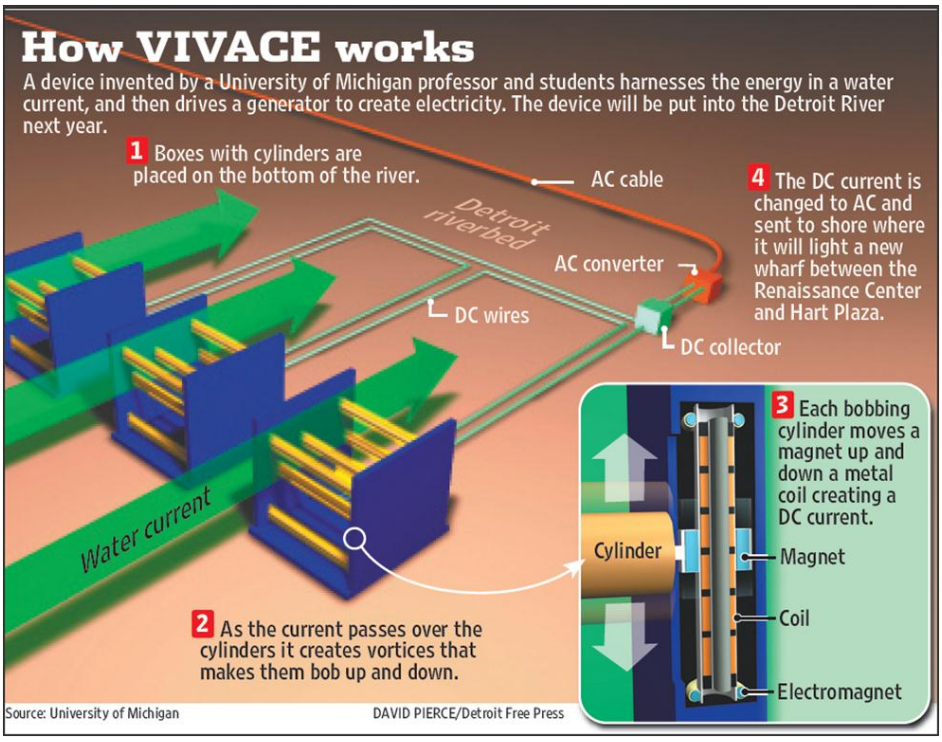

Figure 4 - Overview of the VIVACE converter operation [5]

VIVACE is a new concept for generating power that is clean and renewable [6]. Thorough testing of the VIVACE converter reveals that it satisfies the requirements set by the California Energy Commission and the U.S Departments of Energy [24]. Some of these requirements include being unobtrusive to its environment and being based on readily available technology that has a life span of at least 20 years. Additionally the converter can be used year round, has the ability to generate power with a high energy conversion ratio even at low speeds [7], and is easily compatible with the current electrical grid. VIVACE also believes there is great room for improvement in terms of optimizing vortex shedding, damping, and configurations of arrays of systems.

The benefits of a VIV-powered power system are numerous. Such a device would be able to take advantage of flows that are much too slow to drive a typical turbine-type hydroelectric generator. These slower flows are found all over the world in the form of tidal flows and rivers.

2.3 Review of Previous MQPs

This is not the first time the idea of harnessing energy from an object undergoing vortex induced vibrations has been investigated. In 2011, two MQP groups attempted to accomplish this goal. The first group was comprised of Hall-Stinson, Lehrman, and Trapp [10] and the second group consisted of Distler, Johnson, Kielbasa, and Phinney [11]. The work completed by both groups provides solid base on which to found this project, however their final results leave a great deal of testing to be completed and verified.

Both groups compared their results to those of three sources in order to compare their legitimacy. First, they looked at previous studies of VIV power harnessing to get an idea of

expected results. Then, they created math models to calculate all the necessary parameters. Finally, they executed the physical testing and then compared the results of each finding to ensure similarity. As for the differences in the two projects, the most prominent was the idea of experimenting with different shapes to obtain lift forces and, in turn, shedder displacements that closely resembled the results of current research, like VIVACE. The first group of Hall-Stinson, Lehrman, and Trapp decided to test only cylindrical shapes and just vary the diameter [10]. The second group of Distler, Johnson, Kielbasa, and Phinney made the decision to find an optimized shape that would provide large lift forces and amplitudes [11]. They suggested a curved T shape would increase lift. In the end, both teams ran into issues of low displacements and forces, low power output, and the inability to achieve lock-in frequency. Both groups agreed that two experimental components prevented them from getting desired results. First was the limit in the attainable flow velocity, with measured flow velocities of less than 0.5 m/s. Next, was the issue of the spring stiffness in the oscillator system. The system needed to have an adjustable natural frequency, which required many springs of different stiffness. In addition to being adjustable, the springs needed to have a very low stiffness to obtain the correct natural frequency.

2.4 Flow Systems

Before beginning the design and construction of an improved flow system, research was conducted to identify and compare the many types of conventional water tunnel designs.

2.4.1 Head Tank

One of the major components present in many hydrodynamic research facilities is a constant-level head tank. Regardless of the type of test system, a constant-level head tank provides steady flow by using gravity to provide water pressure to the test rig. Head tanks are found in both academic [25, 26, 27] and commercial [28, 9] hydrodynamic laboratory

environments. A head tank allows the system to absorb any pump noise that may be present in direct-pump piping configurations. It also allows the pressure supplied by the head tank to be easily calculated, based on simple hydrostatic pressure:

$$Head\ Pressure = \rho g \boldsymbol{h} \quad \textbf{Equation 5}$$

where ρ is the fluid density, g is the gravitational constant, and h is the height differential between the water level in the head tank and the outlet pipe exit.

2.4.2 Types of Water Tunnels

There are several types of open-channel water tunnels that were considered for the design of this system. One of the more popular water tunnel designs is the variable-slope flume. These flumes are available commercially [29] and offer some distinct advantages. These types of flumes have very uniform flow through the test section because they are long and can be fitted with stilling components (flow straighteners). A uniform flow profile is essential for VIV testing because the shedder traverses across the test section width. The tilting flume also allows fine control over the water level by means of a weir at the downstream end. While some flume models incorporate constant-level head tanks, the majority use floor-level pumps to recirculate the water.

Figure 5 - 10M Research Flume - Purdue University, USA [29]

Another type of design uses a directly-connected motor and impeller to move fluid in a recirculating tank. An example of this kind of system is the Low-Turbulence Free Surface Water Tunnel at the Marine Hydrodynamics Laboratory at the University of Michigan [30]. Figure 6 shows a schematic of the water tunnel.

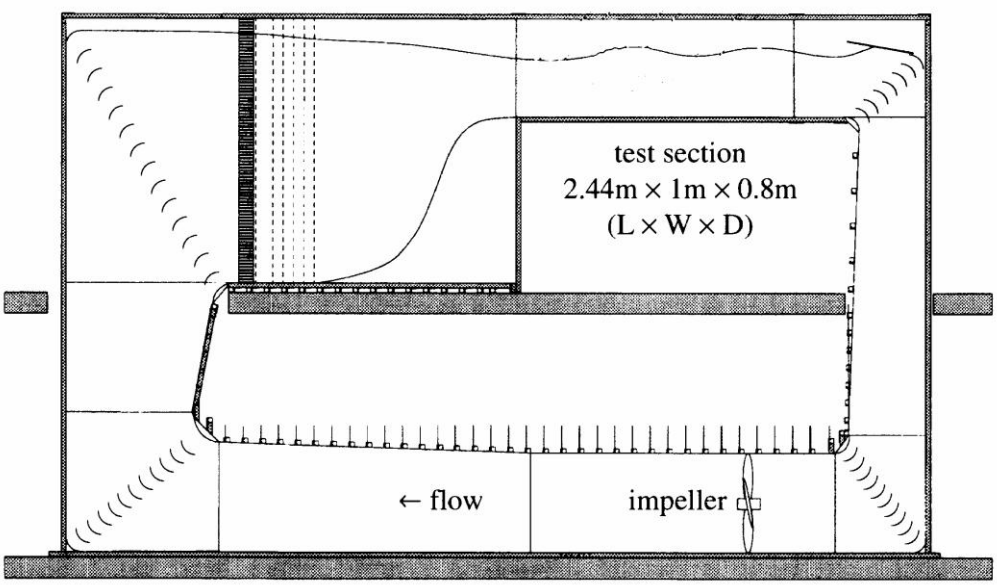

Figure 6 - Schematic of LTFSW Channel (Reproduced from Walker et. al. [31])

These two types of open channel water tunnels have advantages when it comes to generating the desired flow in the test section. They are very effective in producing a steady, uniform flow, due to some of their fine-tuning abilities, like the slope in the tilting flume and the impeller speed in the recirculating water channel. But there are disadvantages present with these designs in terms of space requirements (tilting flume needs to have considerable length to allow the flow to stabilize at the test section) and expense. These are the two reasons these designs were ultimately not chosen as the final flow system design.

2.4.3 Submerged Jets

To develop a steady flow profile submerged jets may be used in the final design of the flow system. A team of researchers presented a formula that would describe the velocity profile of a submerged jet with a large exit [20]. The incompressible flow of a small-scale exit submerged jet typically has a velocity profile similar to a Gaussian distribution. The velocity at

the initial region of flow development is relatively small compared to the fully developed region The formula for small-scale exit submerged jets is shown in equation 6.

$$u = u_m * e^{-\left(\frac{r}{b^*}\right)^2}$$ **Equation 6**

Where u is the velocity on cross section of submerged jet, u_m is the velocity on the centerline of jet, r is the radial coordinate, and b^* is the spreading width of jet flow velocity.

When the exit of the submerged jet is significantly large, like the propeller jet of a ship, the initial region of flow development cannot be neglected. Equation 7 shows the derived formula for a submerged jet with a large exit.

$$u = u_m * e^{-\left[\left(\frac{r}{b^*}\right)^2\right]^{\xi(x)}}$$ **Equation 7**

Where $\xi(x)$ is a radial adjusting coefficient, which is a function of the jet flow direction, x. It was concluded that the distributions of the velocity profile calculated from the new formula fit the data well. This formula was acceptable in estimating the velocity of jet flow in both the initial and fully developed region [20]. Figure 7 below shows a schematic of the flow profile, with several variables that define different aspects of the shape and velocity of the jet.

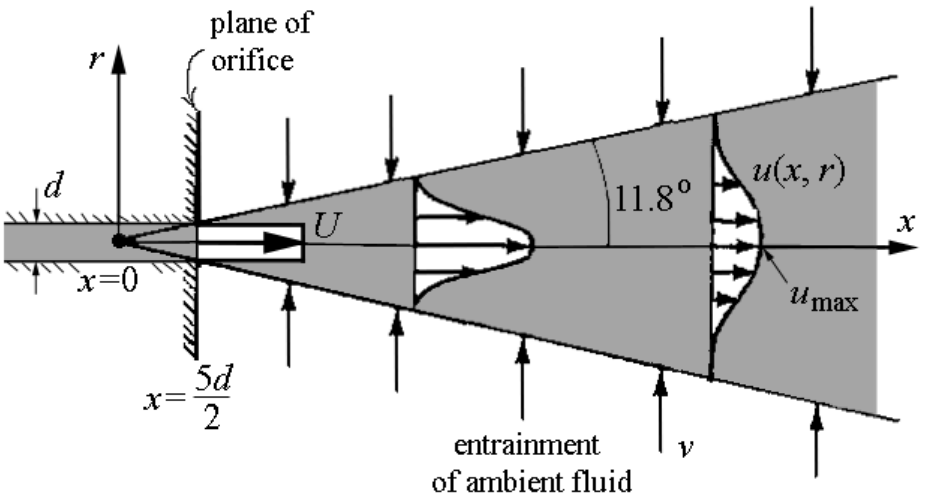

Figure 7: Schematic of Flow Profile downstream of a submerged jet exit.

One of the requirements for the exit flow of the diffuser is that the flow profile be uniform, for this is the flow that will be passing over the vortex shedder. Equation 8 shows the radius of the jet with respect to distance downstream.

$$R(x) = \frac{1}{5}x \qquad \textbf{Equation 8}$$

Where, *R* is the jet radius at some downstream distance *x* from the discharge location [21].

2.4.4 Diffusers

To develop a steady flow profile over the test section a diffuser may be used in the final flow system design. One of the biggest considerations when designing a diffuser is the angle of expansion. If the angle is too great, flow separation may occur and can cause non uniform flow to exit the diffuser. Conventionally, conical diffusers are designed with a wall expansion angle of 5-6° [17,18]. The only drawback with using a diffuser with an angle of 5-6° is the resulting length of the component when a large area ratio is required. Wide-angle diffusers reduce the length of a diffuser of a given area ratio [17], while still converting the flow's kinetic energy into

pressure energy with minimum loss [18]. As mentioned above, a large diffuser angle leads to flow separation, so one cannot simply increase the angle and expect it to match the performance of a small angle diffuser. Through experimentation and testing, it has been shown that an effective way of preventing separation in a wide-angle diffuser is by introducing perforated metal plates or wire gauze [19]. In 2004, the University of Sydney in Australia investigated the use of perforated plates to control the velocity distribution at the outlet of a 30° wide-angle diffuser. Wide-angle diffusers are used extensively in wind tunnel design. From the study, it was concluded that for a 30° wide-angle diffuser with an area ratio of 7, incorporating two screens, each with a porosity of 45%, at positions 34.25 mm and 130.15 mm from the diffuser inlet yielded a uniform velocity profile exiting the diffuser [19].

3.Methodology

3.1 CFD

To get an idea of expected amplitudes and frequencies of the geometries that will be tested experimentally, a theoretical analysis via computational fluid dynamics (CFD) was performed. The computational tool that performed the best overall was the flow simulation package of Solidworks 2011.

The first step that needed to be completed in the Solidworks Flow Simulation analysis was to create the 3D model of the geometry. A two-dimensional sketch of the geometry's cross section was drawn, assuring the sketch dimensions matched the dimensions of the physical shedder. Next, parameters like units, fluid properties, analysis type (external), run duration and time step, and boundary conditions were imported using the flow wizard feature. Final steps involved setting the computational domain, choosing simulation type (two-dimensional),

selecting mesh resolution, and specifying desired goals, i.e. parameter to calculate, for the simulation (Y-component of force). Also, a goal plot was set up to output the force values against physical time. Since the intended purpose of using CFD was to obtain plots of lift coefficient and Strouhal number versus Reynolds number, the batch run feature was utilized, which allowed for multiple configurations to run simultaneously. Each configuration had a different velocity, and hence a different Reynolds number. The range of Reynolds numbers tested were 2000, 4000, 6000, 8000, 10000, 12000. See Appendix D for the specific velocities used to acquire the corresponding Reynolds number for each shape's set of data.

After the force versus time plot was generated for each Reynolds number, the constant peak force was determined. To accurately compare lift of each shape, those values were then normalized to C_l and a subsequent lift coefficient versus Reynolds number plot was created for that particular geometry. The lift coefficient per unit span normalizes the lift force of an object by relating it to the dynamic pressure of the fluid and its cross-sectional area. Equation 9 is as follows

$$C_l = \frac{\frac{L}{b}}{.5 * \rho * U^2 * c} \quad \textbf{Equation 9}$$

where L is the total lift (the value taken from the force versus time plot), b is the length (the lengthwise computational domain dimension), ρ is the density of water (998 kg/m^3), U is the fluid velocity, and c is the characteristic length (see Figure 8).

In addition to calculating lift coefficient, the Strouhal number was found using the frequency of the force versus time curve. The Strouhal number is similar to the lift coefficient in that it non-dimensionalizes the oscillations of an object in a flowing fluid. The equation for Strouhal number is

$$St = \frac{f * c}{U}$$ **Equation 10**

where f is the frequency of vortex shedding, c is the characteristic length (see Figure 8), and U is the fluid velocity. The Strouhal numbers were then plotted versus Reynolds number.

Finally, the lift coefficient and Strouhal number curves for each shape, cylinder, 1.5:1, 1:1, and curved T, were then superimposed on the same plot for comparison.

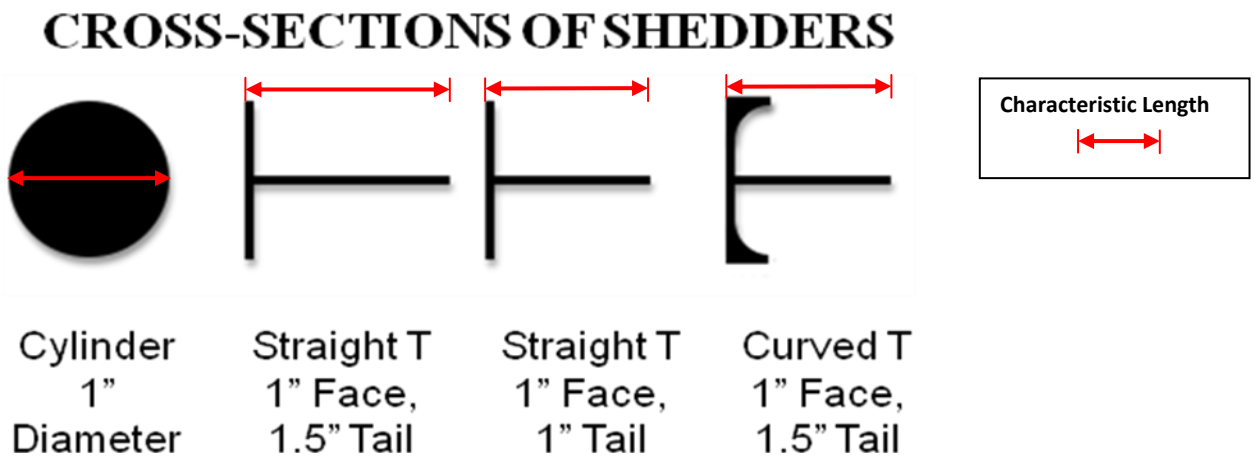

Figure 8: Cross-section of geometries tested in CFD and experimentally

3.1.1 CFD Results

The following section showcases some of the capabilities of SolidWorks Flow Simulation in terms of analysis goals and visual accompaniment. SolidWorks Flow Simulation was able to provide the y-component of force versus physical time plot for the 4 geometries tested and a corresponding pressure map, showing the various pressure values in the flow. The force versus time result was the primary reason for using computational fluid dynamics, whereas the pressure map is mainly for educational purposes, showing an interesting perspective into what causes the object to oscillate.

For each set of force versus time and pressure map screenshots shown below, total analysis time was 30 seconds and the fluid velocity was .175 m/s. This is the approximate velocity of the water in the test area of the flow tank. The corresponding Reynolds number is different among each shape, since the characteristic length varied, but on average, it is 6,450.

The final two plots in this section show the collection of lift coefficient and Strouhal number as a function of Reynolds number for the 4 geometries.

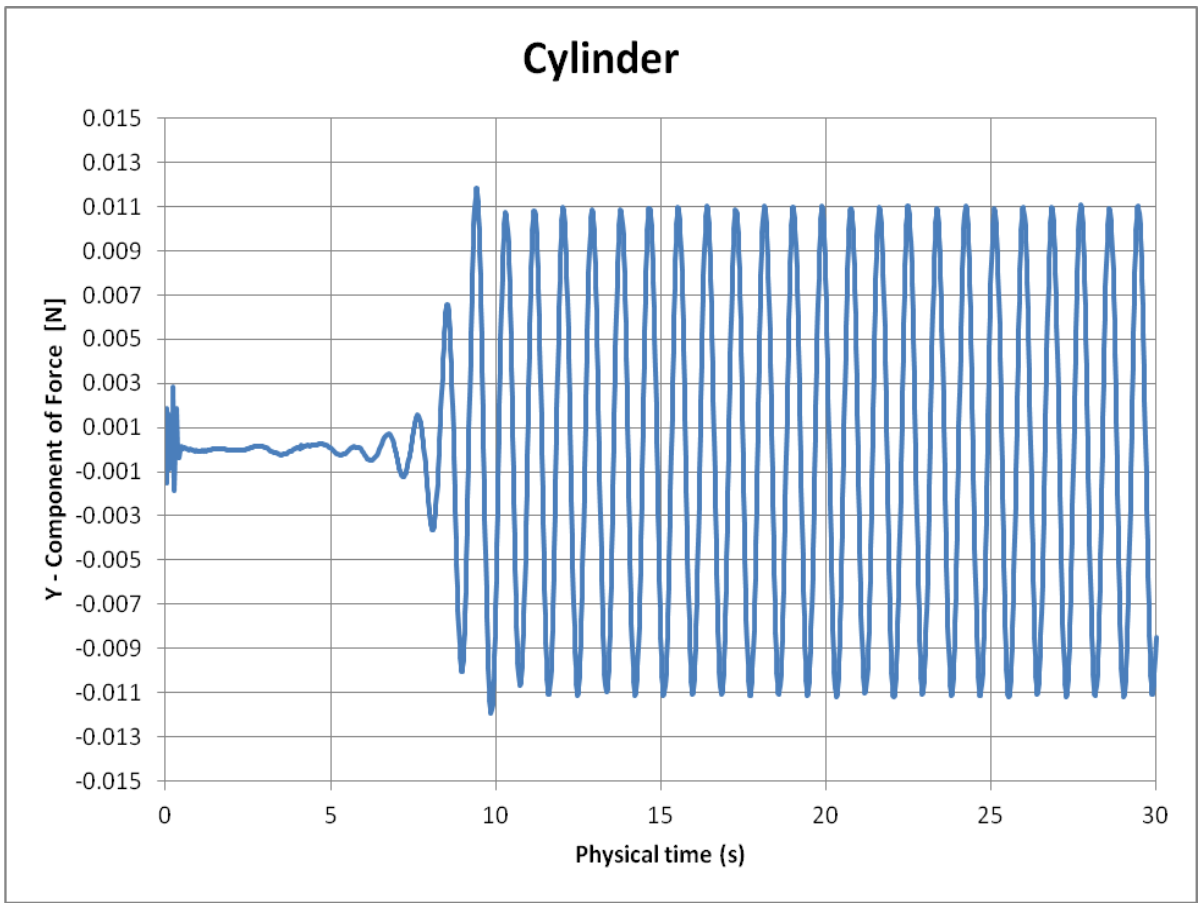

Figure 9: Cylinder Y Component of Force Vs. Physical Time

Figure 9 shows that the cylinder does not start to stabilize its oscillations until around 10 seconds into the run. At this point the peak y-component of force, amplitude, remains fairly constant at a value of .011 Newtons. The curve also stays relatively sinusoidal in nature, and yields a frequency of around 1.14 Hz.

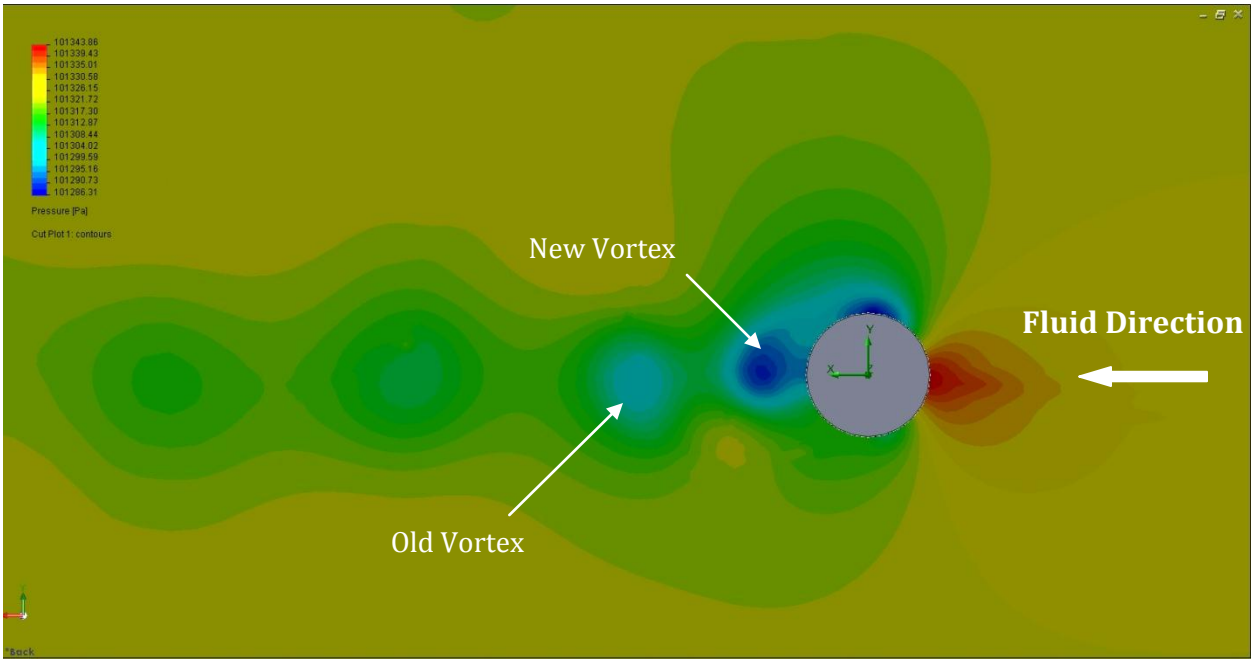

Figure 10: Cylinder Pressure Map at Maximum Lift

Again, this pressure map shows the different pressures in the moving fluid at the time instant where the cylinder experiences maximum lift. As expected, a distinct vortex is created on the upper side of the cylinder, and is represented by the dark blue region just downstream of the cylinder. It is an area of low pressure and will cause the cylinder to move in its direction. The light blue region to the left of that newly created vortex represents the remnants of the old vortex that was present on the lower side of the cylinder just moments before. The spectrum of colors in the top left corner of the screenshot show the corresponding pressure value for the various colored regions of the pressure map. Note that the pressure value difference between the dark blue and green shades is 26.56 Pa.

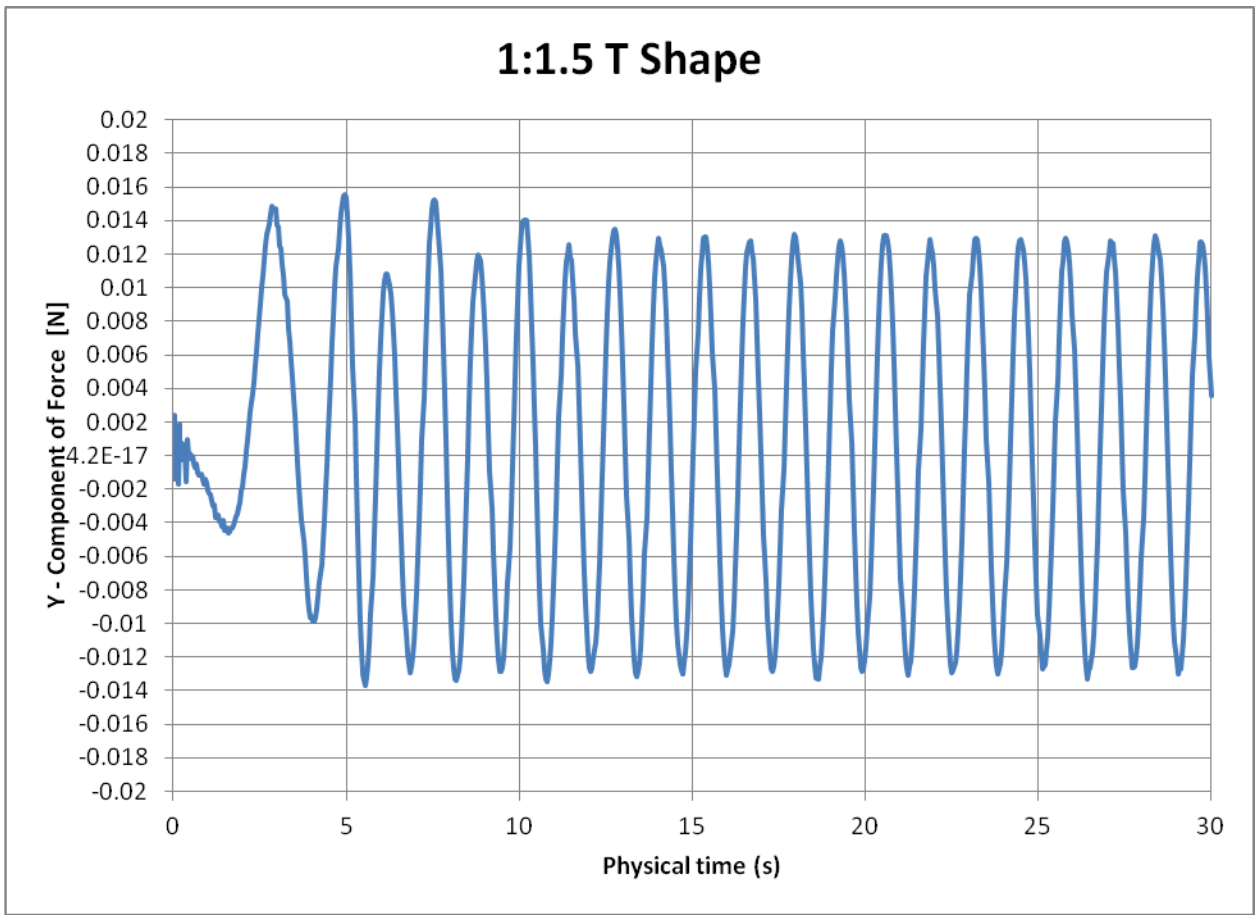

Figure 11: 1:1.5 T Shape Y Component of Force Vs. Physical Time

Figure 11 shows that the 1:1.5 T shape reaches a "steady" state much earlier than the cylinder: around 5 seconds into the run. But it takes until about 10 seconds in for the y-component of force to level out at a value of .013 Newtons, with the overall frequency of the signal equaling 0.78 Hz.

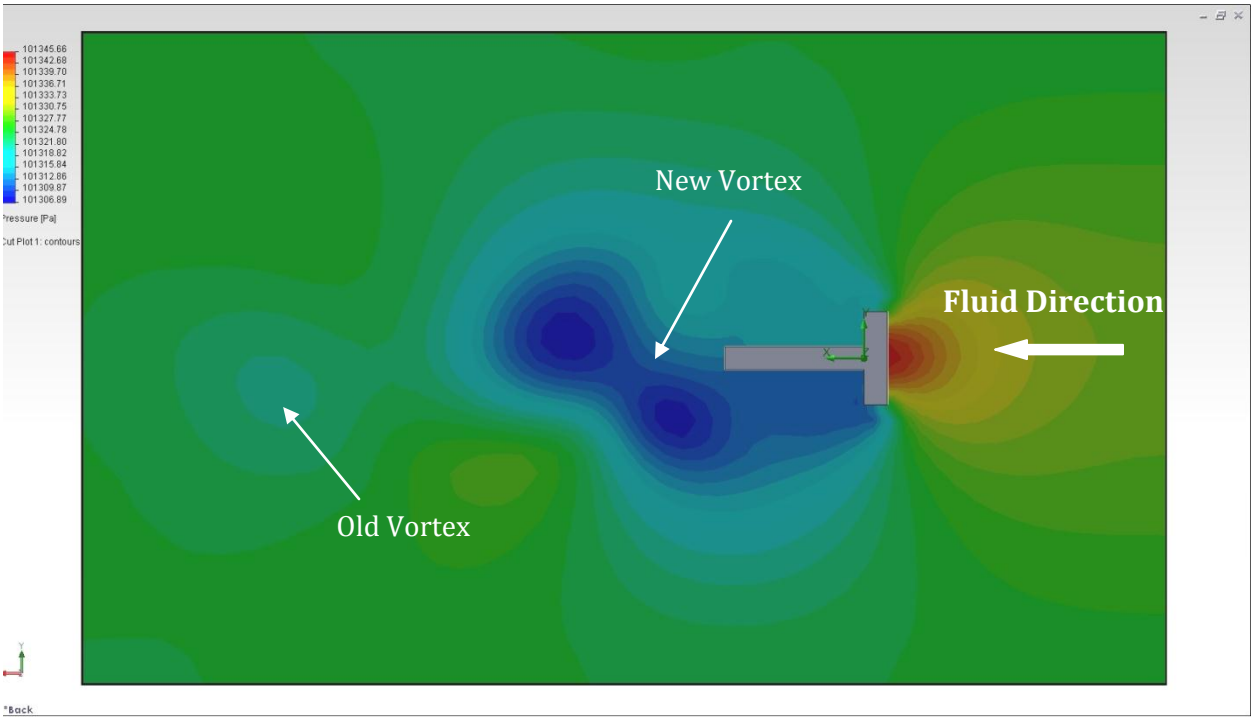

Figure 12: 1:1.5 T Shape Pressure Map

In this pressure map of the 1:1.5 T shape, the vortex created on the bottom side is much more sizeable than the vortex from the cylinder. Again, the remains of the previous, top side vortex can be seen downstream. In this case the pressure difference in the fluid between the top and bottom of the T, taken from the pressure legend at the top left corner, is 11.93 Pa. This correlates with the lower y-component of force value in comparison to the cylinder, which had a higher pressure difference and thus a higher force value.

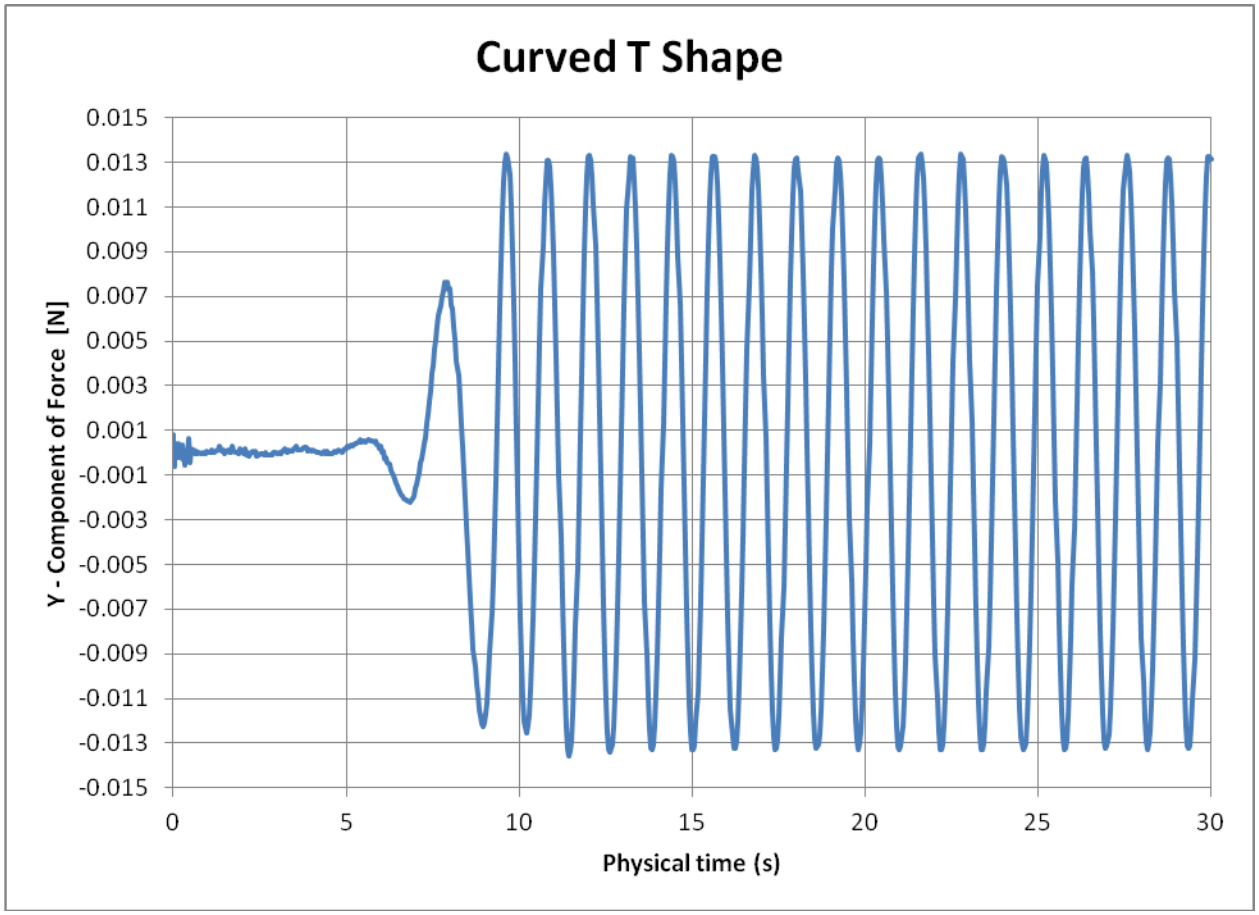

Figure 13: Curved T Y Component of Force Vs. Physical Time

Like the cylinder, this graph show that the oscillations of curved T shaped even out at around 10 seconds into the simulation. The analysis has revealed the lift force to be around .013 Newtons and its shedding frequency to be 0.83 Hz. It seems the curved feature does not make any significant improvements to the shedding frequency or even the lift force. But only when lift coefficient is found for all the shapes can a better assessment be made about lift characteristics in terms of largest and smallest amplitudes.

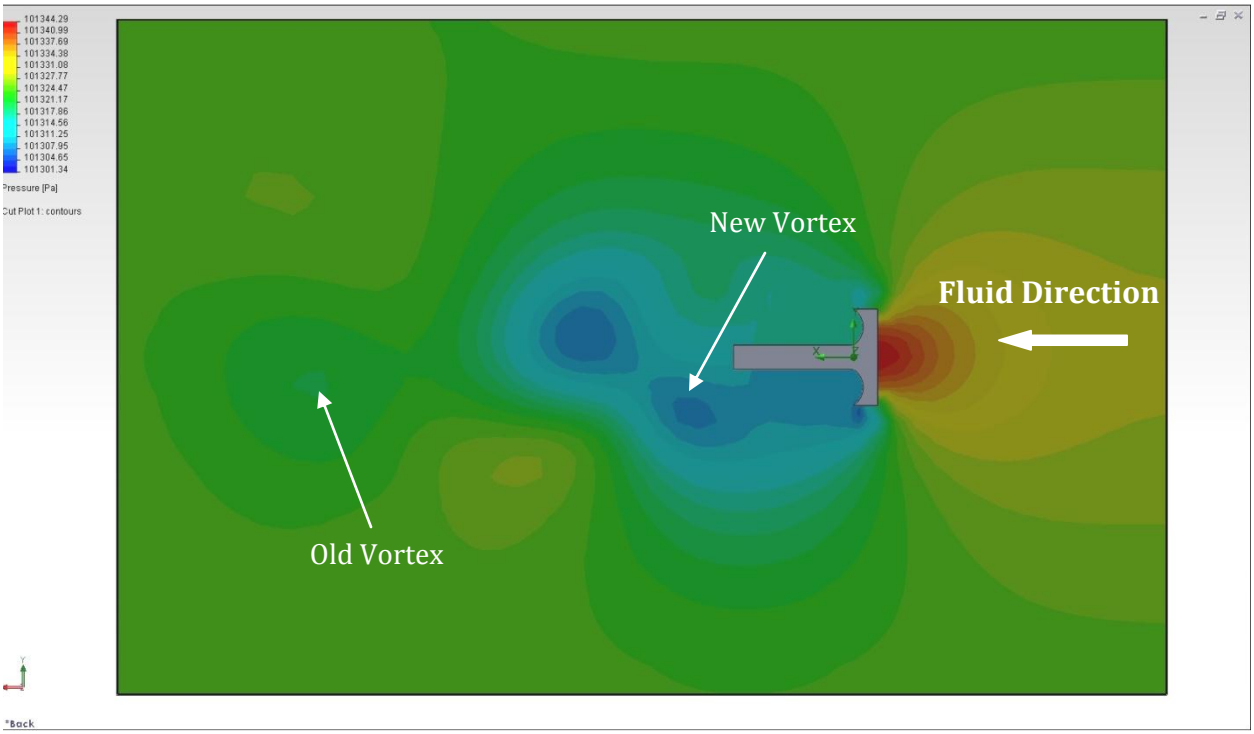

Figure 14: Curved T Pressure Map

In Figure 14, the curved T shape has a similar low pressure form, with a double vortex pattern trailing off the lower portion of the geometry. The two aspects that make this pressure map noticeably different from the 1:1.5 T and even the cylinder are the intensity of the "new" vortex and the lack of an obvious "old" vortex. The two areas of deep blue clearly indicate the location of the vortices, but this shade of blue does not appear to reach the deepest blue in the color spectrum like the cylinder and straight T had. Therefore, the "old" vortex that formed moments before quickly fades into the greenish shade. The green shades of color indicate the pressure in steady state. From the force versus time plot above, it can be seen that the lift value for the curved T is approximately the same as the straight 1:1.5 T. The pressure difference from the screenshot matches this similarity, for the change in pressure from the top to the bottom side of the geometry is around 9.91 Pa.

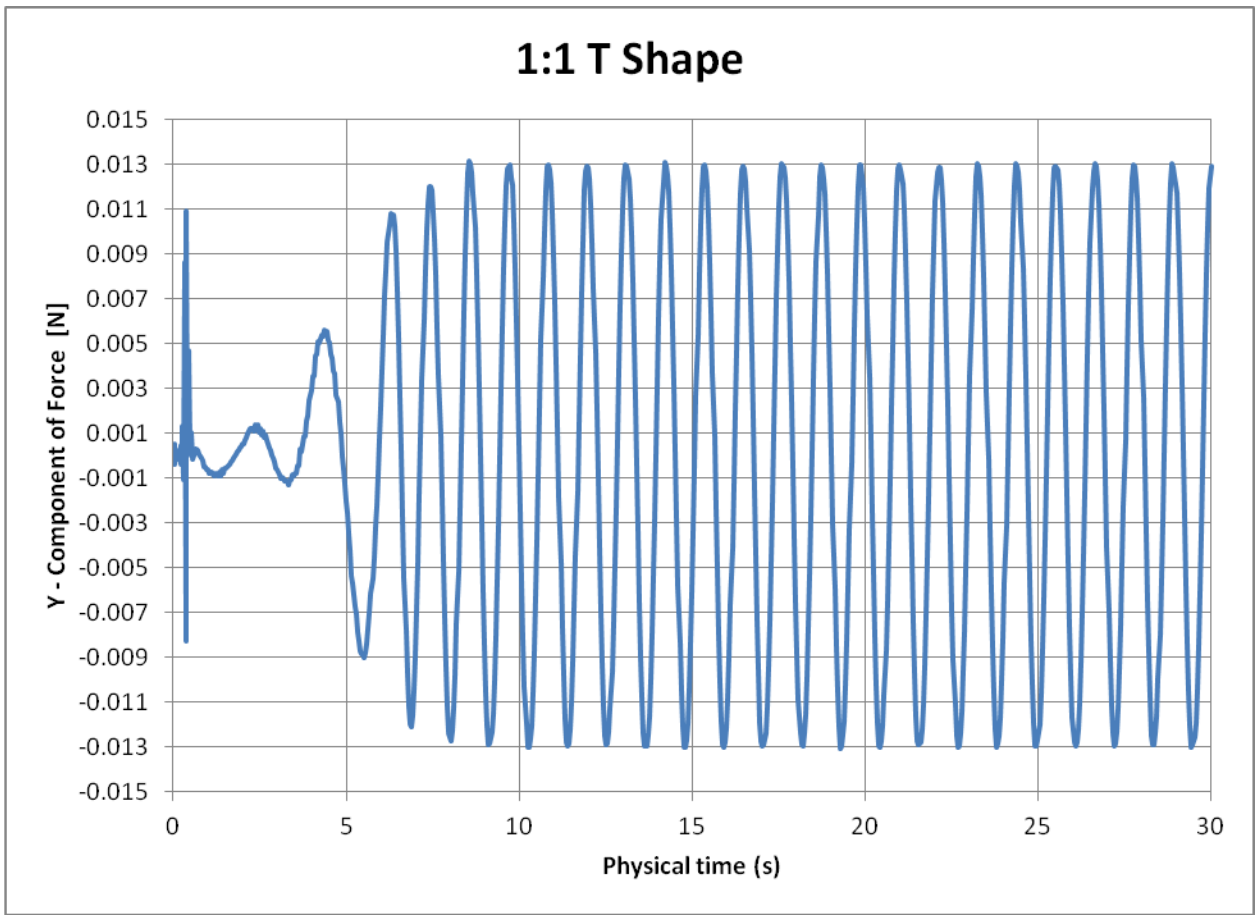

Figure 15: 1:1 T Shaper Y Component of Force Vs. Physical Time

Once again, the y-component of force for the 1:1 T shape is .013 Newtons. Its shedding frequency is 0.86 Hz, the highest of the three T shapes. As stated above, though, a decision cannot be made about the best candidate for highest amplitudes until a lift coefficient is calculated.

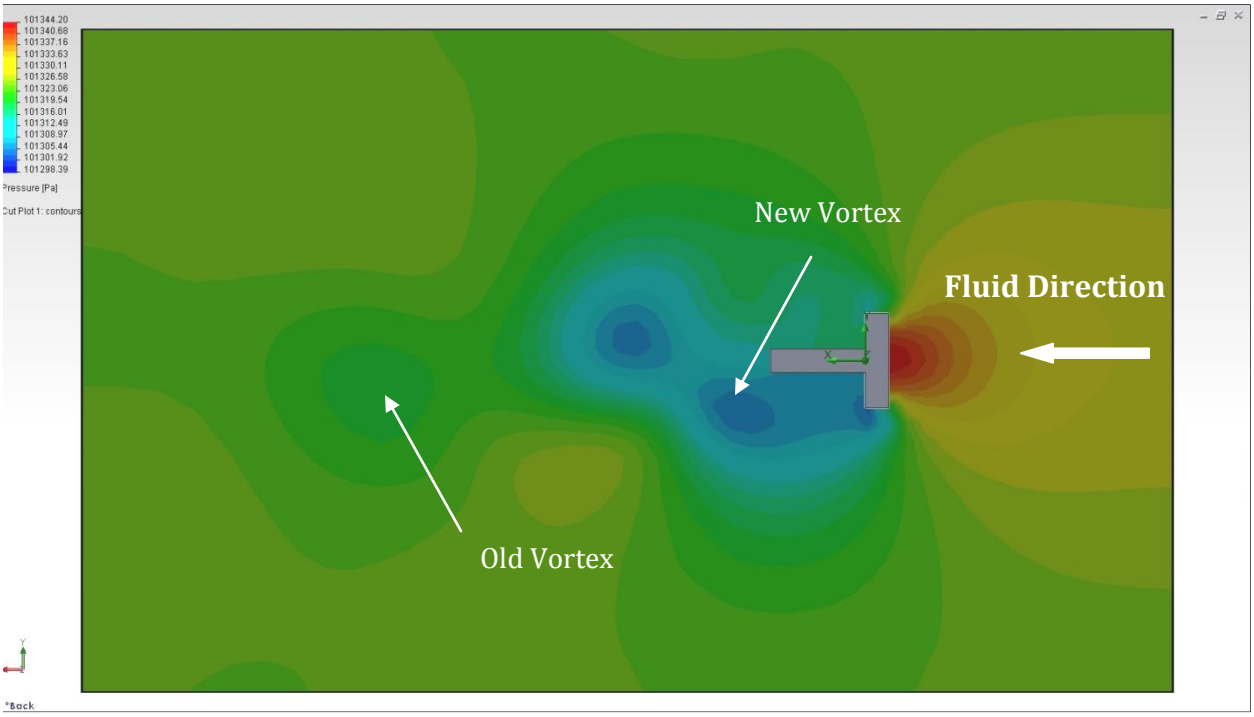

Figure 16: 1:1 T Shaper Pressure Map

The layout of this pressure map is very similar to that of the curved T shape. The same statements can be about the intensity of the "new" vortex and lack of an obvious "old" vortex. Since the peak force value for this 1:1 T shape was essentially equal to that of the 1:1 and curved T, it is expected that the pressure difference would also be comparable. It is similar, with a pressure difference between upper and lower surface equal to 10.57 Pa.

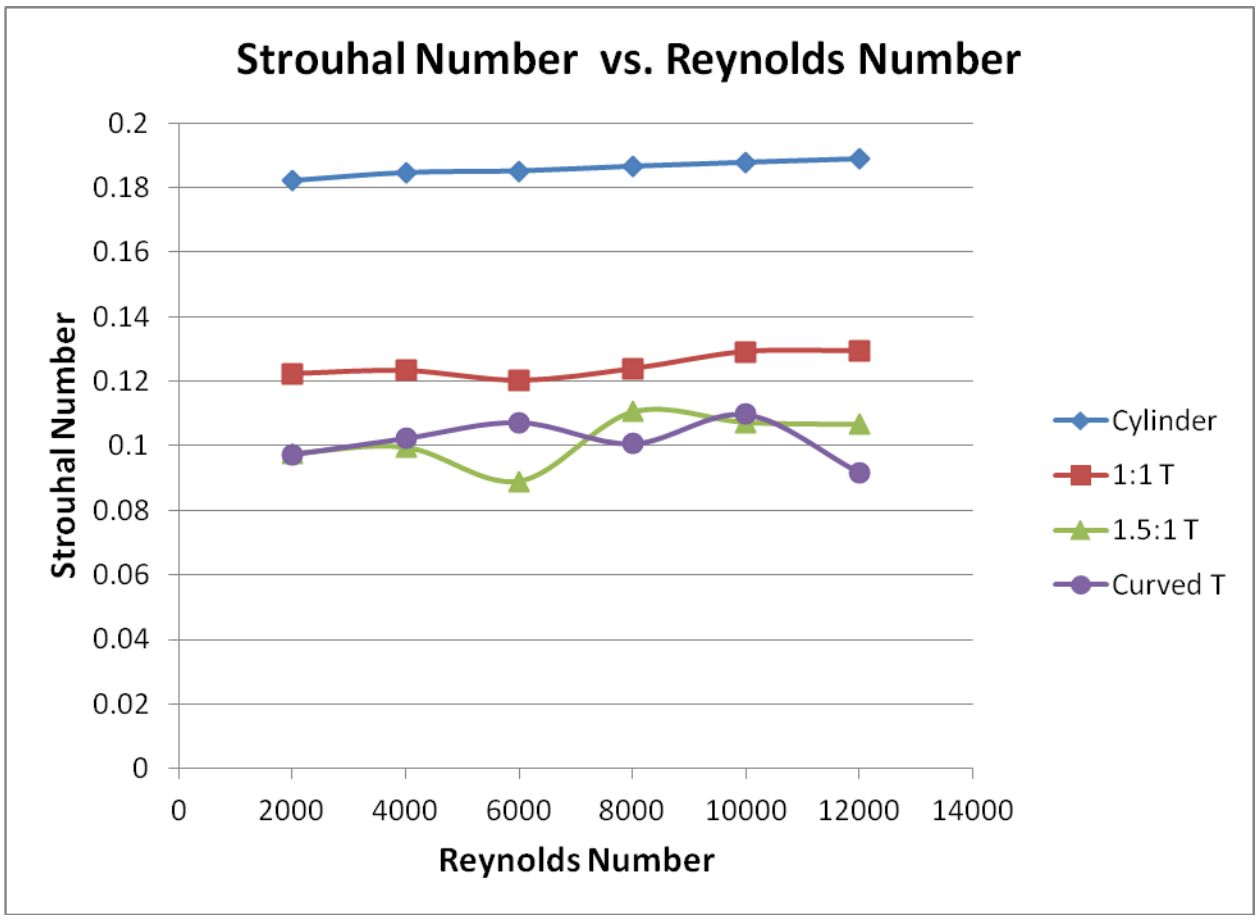

Figure 17: Strouhal Number for all Geometries Over a Range of Reynolds Number

The aggregate plot in Figure 17 shows the Strouhal number for each shape when simulated over a range of Reynolds numbers. They all have a relatively constant value, with the cylinder having the highest average Strouhal number, and the 1:1.5 and curved T having virtually the same, lowest average Strouhal numbers. This Strouhal number data was ultimately used in the lock-in calculations for the experimental testing. And it will be seen from the experimental results that the oscillation frequencies for each shape follow the same trend as these theoretical Strouhal number results, with the cylinder having the highest frequency, and the other shapes having frequencies about half of that.

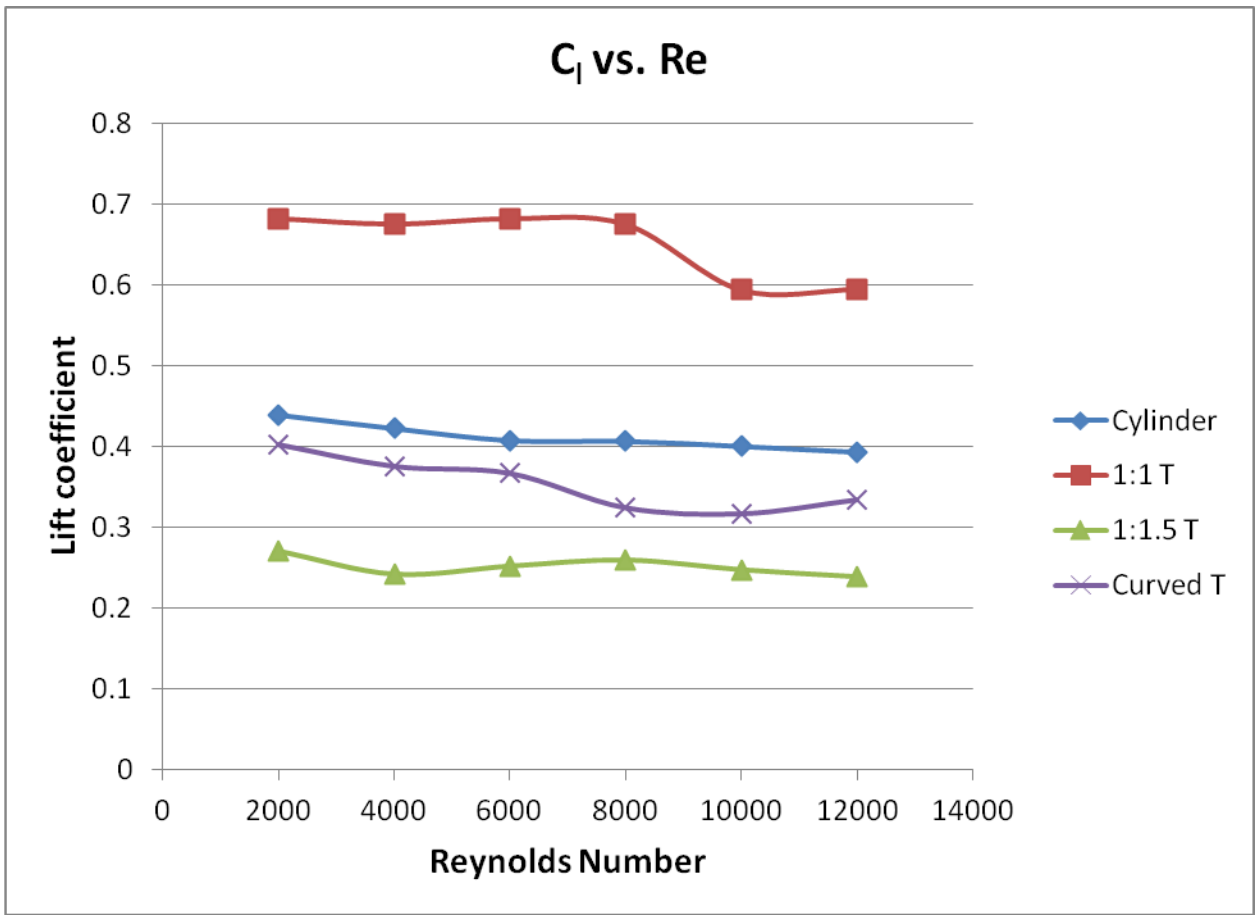

Figure 18: Cl for all Geometries over Reynolds Number

Clearly, from Figure 18, the geometry with the highest lift coefficient is the 1:1 T shape, and this revelation will again correlate with the results from the physical tests, with the 1:1 T yielding the largest amplitudes. See Appendix D for detailed CFD results and input parameters for the simulations.

3.2 Flow System Design

The design of the flow system was based on the ISO standard for flow measurement [8] and a layout/construction plan for use at the Physikalisch-Technische Bundesanstalt (PTB) test facility in Braunschweig, Germany [9], whose distinguishing features include precise flow control and stability. The aforementioned design describes a close-conduit type flow test section, for use with inline flow meters and other devices. For this studies test section, an open-channel type area is needed to simulate real-world flow conditions.

The flow system is a closed loop, starting with a head tank. The head tank is located some distance vertically above the test section in order to supply hydrostatic pressure to the test section. The head tank has a wide girth, thereby minimizing the change in water level due to variations in the supply flow rate, allowing us to neglect the head pressure changes as a result of changes in water level.

From the head tank, a pipe section delivers flow to the test section, fed by gravity. Since the water level in the head tank is constant, one can expect a constant flow rate through this pipe section. In order to control the flow rate in the test section, the pipe section will include a control valve.

The test section was constructed using a 6’x2’x2’steel oval test tank from a previous MQP. This test tank will be split longitudinally by means of a solid partition that spans the straight portion of the tank. The incoming flow from the head tank will be connected to a submerged diffuser, which develops and expands upstream of the test section. The test section is located some distance downstream of the diffuser. This distance will ensure that the flow has time to fully develop into a uniform flow profile before crossing the test section. Downstream of the test section, the flow is then directed around the bend in the test tank, and reverses the flow

180° on the other side of the partition. The flow traverses the length of the test tank, where a system of water pumps transfers fluid back to the head tank. To prevent excess fluid from accumulating in the head tank, an overflow pipe was fitted to the head tank. This serves to keep a constant water level in the head tank, and provide a constant velocity.

There are several advantages to using this flow system design. The flow rate in the test tank is controllable by a single control valve. The fluid levels in both the head tank and test tank are completely independent of the flow rate, and therefore do not need to be adjusted to prevent overspill. The pressure from the head tank is gravity controlled to avoid instability in pump flow rates that would otherwise affect the flow rate in the test tank. One of the drawbacks of this system is that the pump system capacity must be greater than or equal to the flow rate from the head tank. This will ensure that the head tank level does not drop, and change the pressure thereby changing the flow rate at the test tank.

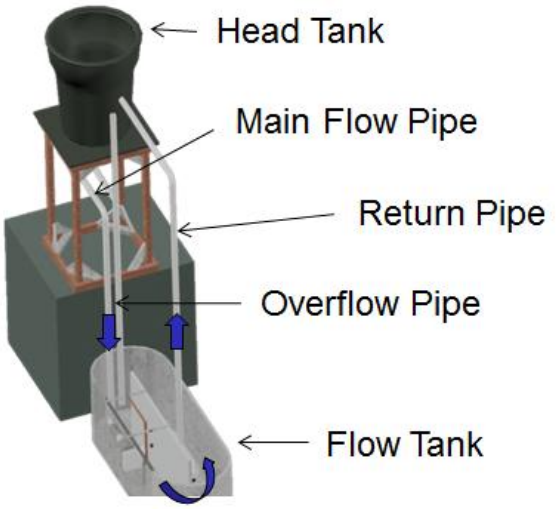

Figure 19 - CAD Overview of Flow System Design

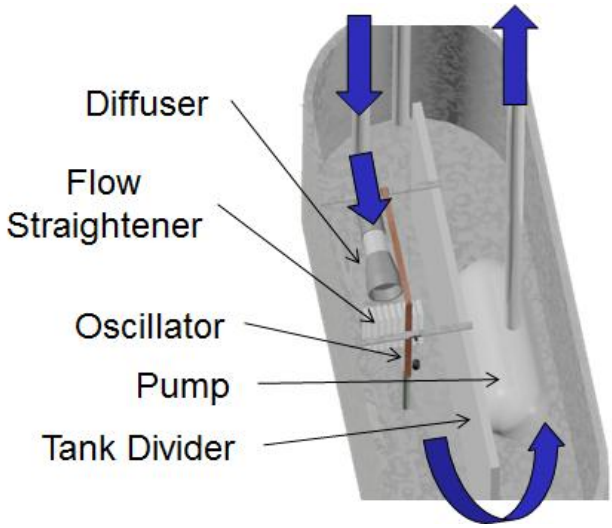

Figure 20 - CAD Overview of Test Tank

3.2.1 Flow Resistance Calculations

Based on the general design of the flow system, a feasibility study was performed to ensure that such a system would fit within the confines of both the available space in the lab, and the monetary budget. In order to determine the required performance specifications of the pump system, the maximum flow rate into the test tank needed to be calculated. The other major feasibility concern was the required height of the head tank water level.

A mathematical model was constructed to estimate these two main parameters (Appendix A). The first approximation involved in the model is the desired flow rate. Based on the previous MQPs [10-11], assume this velocity to be

$$V = 0.8\frac{m}{s}$$

Another design parameter was the exit area of the diffuser. We assumed the diffuser exit to be circular, with a diameter of 6 in. The porosity of the perforated plate/screen at the end of the diffuser is also taken into account using a porosity term, in this case 0.5 (50% open area).

$$D_{diffuser} = 6\ in$$

$$Porosity = 50\%$$

These calculations revealed a needed pump capacity of around 7,000 gph.

To find the required head tank height, losses for each of the flow disturbances were calculated and added to the required head for frictionless flow based on Bernoulli's energy equation. The losses included in the analysis are:

1. The entrance losses at the interface between the head tank and pipe.

2. The 90° elbow that redirects the vertical pipe from the head tank to the horizontal diffuser.
3. The losses for the diffuser assembly, as a combination of the diffuser itself and the perforated plate/screen.
4. The friction losses for flow through the pipe lengths.

The minor losses (items 1-3 above) were calculated using the minor loss equation [12]:

$$Head\ Loss = K\frac{V^2}{2g} \quad \textbf{Equation 11}$$

where

K = minor loss coefficient

V = flow velocity through the disturbance

g = gravitational constant

The following values of K were used in the analysis [13]:

Entrance: $K = 0.5$

Elbow: $K = 0.3$

Diffuser: $K = 0.3$

Perforated Plate/Screen: $K = 3.4$

The major (friction) losses (item 4 above), were calculated using the Hazen-Williams equation:

$$f = 0.2083 \times \frac{100^{1.852}}{c} \times \frac{q^{1.852}}{d_h^{4.8655}} \quad \textbf{Equation 12}$$

where

f = friction head loss in feet of water per 100 feet of pipe (fth20/100 ft pipe)

c = Hazen-Williams roughness constant

q = volume flow (gal/min)

d_h = inside hydraulic diameter (inches)

For PVC pipe, the Hazen-Williams roughness constant was found to be [14]:

$$c = 150$$

The sum of these losses was then added to the frictionless head required, from Bernoulli's equation:

$$Head = \frac{V^2}{2g} \qquad \textbf{Equation 13}$$

where

V = flow velocity at the diffuser exit

From these calculations, the required head tank fluid level relative to the test tank is:

$$Head\ Tank\ Fluid\ Level\ Height = 1.1\ ft$$

Assuming that the feasibility constraint is the ceiling height in the lab, this required head should not pose a problem.

3.2.2 Head Tank Construction

The purpose of the head tank is to provide steady, consistent flow into the test tank. Since the water level in the head tank is constant, a constant pressure is delivered to the diffuser inlet.

In order to raise the head tank to the correct height (based on the head tank loss calculations), it was necessary to construct a structure on which the head tank would sit. The test

tank was located adjacent to a laboratory bench, which was approximately 36 inches tall. To minimize cost and design complexity, the head tank stand was built on top of the lab bench. This alleviated a large portion of the stand height requirement.

The stand was constructed out of 2 x 3 studs, arranged in two rectangular frames, connected by four vertical posts. A section of engineered wood was placed across the top frame and secured with wood screws. This platform would make up the surface on which the head tank would stand. The head tank is constructed of a modified polyethylene container

3.2.3 Diffuser Construction

Since the main goal is to provide a constant shedding frequency a constant velocity is created across the test section. In order to provide a constant velocity across our test section a diffuser was constructed. The diffuser is submerged in the test tank and located at the end of the main flow pipe. The diffused has a 2" inlet that abruptly expands to a 4" outlet. Screens are fixed to the expansion point and the outlet of the diffuser.

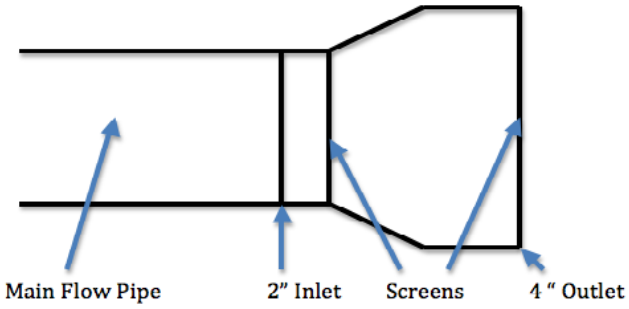

Figure 21: Diffuser Schematic

3.3 Shedder and Oscillator Design

3.3.1 Shedder Design

There were four shedder geometries tested. The cylinder shedder is a simple hollow cylinder. The shedder was constructed with PVC pipe and an end cap to prevent it from filing

with water. The other shedders were made with a rapid prototype machine. They were all variations of a T shape; curved T, 1:1 T, and 1:1.5 T.

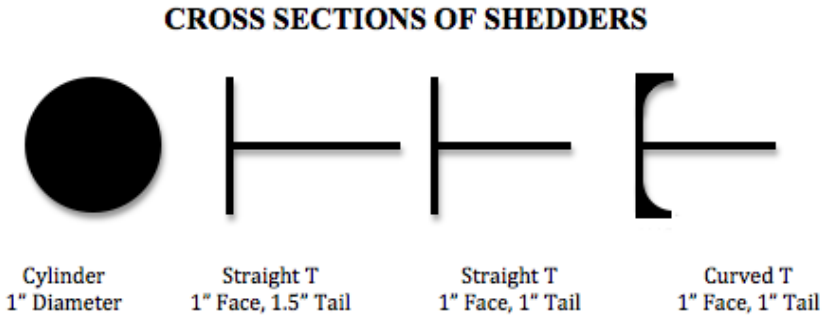

Figure 22: Cross Section of Shedders

3.3.2Drawer Slider Oscillator Design

The oscillator housing involved a frame made from drawer sliders and four pieces of 1x1 inch 80/20 extruded aluminum. The principle idea was to attach each end of the oscillator to a slider, allowing it to move horizontally back and forth along each slider track.

To construct the frame, the largest component of each slider was removed in order to decrease resistance to oscillator motion. Next the second largest component was cut to 10 inches in the machine shop with the use of a band saw to allow it to fit into the width of the test section. The smallest component of the slider, which was referred to as the cart, was then cut to a width of 3 inches with the band saw so that the carts, and in turn the oscillator, could move a greater distance without being stopped by the ends of the sliders. Once the dimensions of the sliders were set, the 80/20 extruded aluminum was cut into four pieces: two 10 inches in length and two 2 inches in length. The two larger pieces were secured to the bottom slider while the two larger ones were secured to the top slider. This provided the opportunity to adjust the height of the

housing by simply attaching the smaller 80/20 pieces anywhere along the larger pieces. This allowed us to accommodate for oscillators of different sizes.

Once the frame was built, the oscillator was attached to determine how effectively it could move in the horizontal direction. While it was able to move back and forth, there was a considerable amount of friction resisting the motion. This was in part due to the deformities in the sliders caused by the clamps that secured them during the cutting process, causing the frame to not be completely uniform. Another likely reason for the friction was the lack of quality in the sliders themselves. Because they are made for heavy drawers which require a much larger force to push than the oscillator, the bearings in the slider were not likely designed for light objects with a relatively weak pushing force. If this design for the oscillator housing were to be used, sliders with less friction in their bearings would be required.

Additionally, four springs could be added by attaching one end near the four junctions of the 80/20 and sliders and the other end to the oscillator. The springs that were to be used would have had to have been very compliant due to the small amounts of force the low-speed water flow produced. The spring constant of these springs was determined by finding the shedding frequency using the maximum Strouhal number that could be attained in this project (roughly 0.2), the flow velocity, and the diameter of the shedder. This shedding frequency was to be used as the natural frequency of the system (in order to achieve lock-in). By knowing this natural frequency and the mass of the oscillator, the required spring constant was determined using the relation

$$f_n = \sqrt{k/m} \quad \textbf{Equation 14}$$

Then the following equation was used to find the necessary spring dimensions.

$$k = \frac{Gd^4}{8nD^3} \quad \textbf{Equation 15}$$

Where,

k = spring constant

d = wire diameter

D = mean coil diameter = outer diameter – wire diameter

G = shear modulus of spring material

n = number of coils

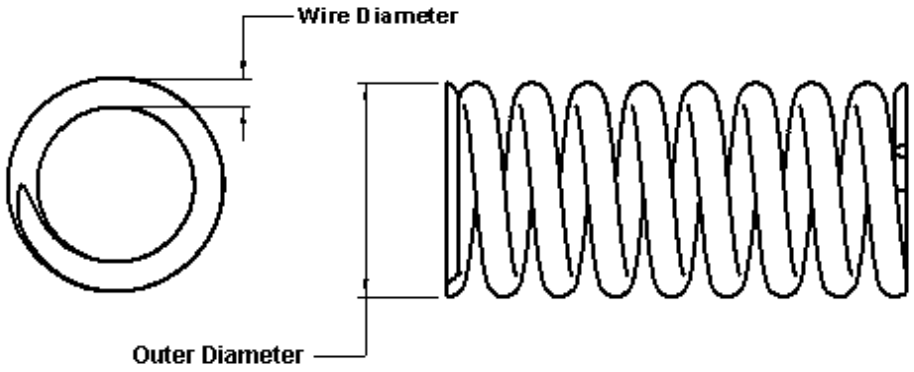

Figure 23: Spring Schematic

Although ultimately this design was not used because it created excessive resistance to motion of the oscillator, a similar design could be used in the future with higher quality bearings.

3.3.3 Second Iteration Oscillator Design and Construction

The pivoting beam oscillator was spawned as an alternative to the slider oscillator while the slider was being constructed. During the assembly phase of the slider oscillator, it was seen that the drag impeded the motion of the oscillator.

Some of the problems discovered were that the cylinder would cease to move at multiple positions in the track due to manufacturing defects and tight tolerances inherent in a ball bearing race. In addition, it required a large amount of force to move even when the oscillator was

already in motion. This translates to a high damping coefficient which was to be avoided in the initial design considerations.

It quickly became clear that the slider oscillator would not suffice for consistent testing. Due to time and budget constraints, it was determined that an alternative should be explored in addition to efforts to improve the slider. The result was the pivoting beam oscillator.

The design is based on a long beam mounted horizontally that is attached to a support structure by means of a pin. On one end of the beam, the cylinder is mounted perpendicular to the beam axis, and a counterweight is attached to the opposite end. The pivot is located closer to the counterweight end of the beam, in order to maximize the length between the fulcrum and the cylinder.

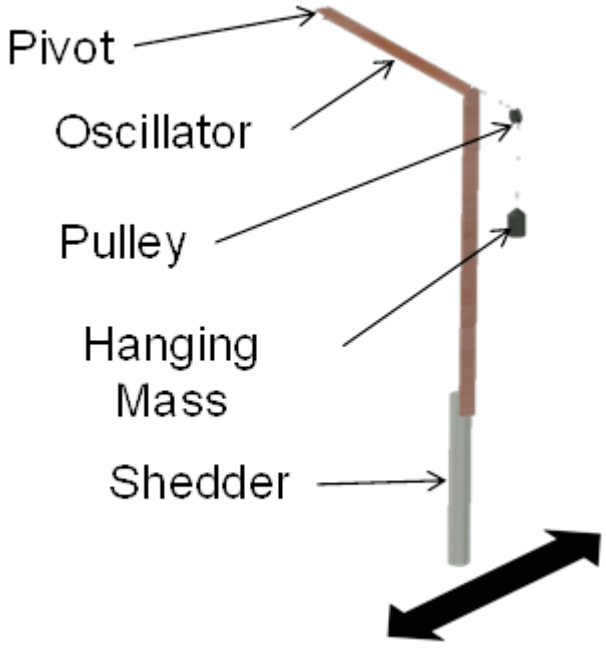

Figure 24: Pivoting Beam Oscillator

Since the cylinder would exhibit circular motion corresponding to large angle deflections of the beam, the distance between the cylinder and the fulcrum was maximized. This has the

effect of producing small angle deflections of the beam, which in turn constrains the cylinder motion to approximately linear motion.

The beam is mounted to the test tank via a rigid cross-member that spans the walls of the tank. The pin is inserted through a hole in the cross-member and the beam. A nut holds the beam up on the pin. The counterweight needs to be adjusted once the beam and shedder are assembled so that the beam is balanced.

Since the beam provides free movement, there is a need for a restoring force to produce an oscillator. In the case of this design, it comes in the form of a thread tied to the end of the beam. The thread is then routed around a pulley located on a test stand outside the test tank. A mass is hung from this end of the thread which provides a restoring force to the location at which the beam and thread are collinear.

This oscillator meets all of the design specifications. Most notably, the beam has very little resistance to motion (low damping) because the only friction is at the interface between the beam and pin. Unlike the slider design, the motion is smooth and consistent. In addition to the motion characteristics, the restoring force is also highly adjustable via the mass that is hung from the thread. Increasing the mass will increase the restoring force and vice versa.

3.3.4 Shedder-Oscillator Design Calculations

Extensive math modeling was performed in order to verify the operation of the shedder-oscillator system under realistic conditions. The main goal of the model was to ensure that the system would be able to provide a range of natural frequencies both less than and greater than the expected shedding frequency for each shedder. The secondary goal of the model was to ensure that the deflection of the shedder from the neutral point would be both sufficient for measurement, but not so large as to exceed the limits of the uniform flow profile or the edges of

the test section. The calculation methodology is described here, while the output is in Appendix B.

The analysis starts with the hanging mass. From this value, the tension force in the string can be found. Since the restoring force depends on y , the displacement of the shedder from the neutral point, a function to describe the force was found. It was observed that the force vs. displacement graph was relatively linear within the range $y = -L$ to $y = L$. This corresponds to a maximum angle in the string of 45°. These limits were chosen as the operating limits for the oscillation displacement. The reasoning for this is that only linear restoring forces could be used to simulate a spring-mass system and use the related spring-mass equations. Therefore, the similarity between a spring-mass system and the hanging mass system is only valid in the range $-L < y < L$. The effective spring constant of the system was determined by finding the proportion between the restoring force, F_y , and the displacement, y.

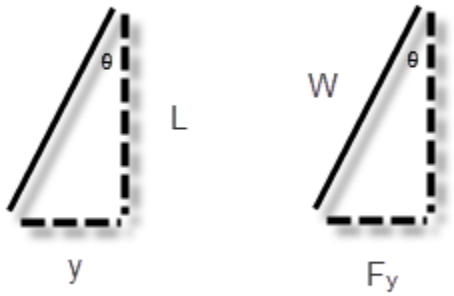

Figure 25: Determining the effective spring constant

$$F_y = W\sin\theta \cong W\tan\theta = \frac{W}{L}y$$ **Equation 16**

Note that in equation 16, $\sin\theta$ was approximated as $\tan\theta$, which is valid for small angles.

In addition to the spring constant, the effective mass of the system was calculated. This included the mass of the shedder and beam, as well as the equivalent mass of the hanging mass, as a ratio of their kinetic energies. An expression was developed for the relation between the motion of the shedder and the motion of the hanging mass.

$$y_m = \frac{y}{sin\theta} - L \qquad \textbf{Equation 17}$$

From this result, a ratio was calculated, as a function of y. The effective mass of the system is then the mass of the shedder added to the ratio of motion times the hanging mass.

$$m_{eff} = m_{shedder} + \frac{y_m}{y} m_{hanging} \qquad \textbf{Equation 18}$$

Using the natural frequency equation for a harmonic oscillator, $\sqrt{\frac{K}{m}}$, a natural frequency of the system was found. With this result in hand, the flow velocity was found that would produce vortex shedding at the same frequency as the natural frequency of the system, thereby achieving lock-in (assuming small damping).

The results of the calculations are presented below:

Hanging Mass = 0.115 kg

Shedder Dimensions: Diameter = 2 cm, Length = 16 cm (Ideal ratio based on VIVACE [15])

Horizontal dist. between shedder and pulley (L) = 7 cm

Total shedder displacement = 11 cm

Ideal flow velocity = 0.97 m/s

Although the ideal flow velocity is a bit high when compared to our estimated flow rate from the head loss calculations, the rate is well within our capability. This is because in order to increase the maximum velocity output of the diffuser, we only need to increase the head tank level. Based on the head loss calculations, we would need only 1.5 feet of head to achieve 0.97 m/s

3.4 Measurement

3.4.1 Flow Rate Sensor

In the flow tank a handheld flow meter was used to measure the velocity of flow in the open channel test section at a chosen point. When the water in the test section passes over the propeller it causes it to rotate. The propeller rotates a magnet that provides a voltage proportional to the velocity of the water. The specific sensor is made by Vernier and simply called a Flow Rate Sensor. The Flow Rate Sensor has a working range of 0 to 4.0 meters per second, accuracy of +/- 1 %, a resolution capable of 0.0012 meters per second, and will provide a full-scale reading in 15 seconds. The Flow Rate Sensor is connected to a DAQ that allows data collection to be done through a computer. The software LoggerPro is used to display real time readings numerically and in graphical form. The propeller is easy to move and therefore can be used to find velocity at almost any location in the testing section. Having the ability to find velocity at multiple points allows us to determine the uniformity of the flow profile.

In order to calibrate the flow rate sensor, a water manometer was connected to a simple pitot tube. The pitot tube was placed into the flow, and the manometer height difference was

recorded. These measurements were made and verified with multiple trials at the same location downstream of the diffuser. The flow rate sensor was then placed into the flow at the test location, and the sensor output voltage was recorded. The calculated velocity value from the pitot tube, along with the sensor output voltage, was then inserted into the LoggerPro sensor calibration as the high point, and zero was used as the low point. This ensured that the measurements taken with the flow rate sensor were accurate. The calibration curve can be seen in appendix E.

3.4.2 Optical Tracking Setup

The optical shedder tracking system was developed to provide instant, accurate position tracking of the shedder with respect to time. The output data from the system can be used to verify oscillatory motion parameters such as amplitude, frequency, and noise.

The system consists of a webcam that is mounted to the test tank main truss, extended in the direction of the shedder-oscillator beam. The camera is directed towards the top surface of the beam some distance away from the pivot point.

A tracking dot, consisting of a rectangular piece of cardboard with a black dot inscribed in the center, is mounted to the top surface of the shedder-oscillator beam. When set up properly, the camera sees only the cardboard background with the tracking dot in the center. At either extreme position, the camera is able to see the tracking dot.

- The Community Core Vision software interprets the video stream and translates the moving tacking dot into spatial coordinates.
- TUIO Mouse, receives the tracking dot coordinates from CCV via the TUIO protocol, and mimics the tracking dot motion with the cursor.

- A third program was written to calibrate the distance traveled of the cursor. The program was also able to record the position vs. time data of the cursor and save it in .csv file format.

The calibration procedure works as follows:

- The shedder-oscillator is moved to the neutral position, and the software is zeroed, thereby setting the offset.
- The shedder-oscillator is moved to the extreme left position, and the software stores this point's coordinates.
- The shedder-oscillator is moved to the extreme right, and this point's coordinates are recorded.
- The software then accepts a numerical value corresponding to the physical distance between the two extremes.
- The result is the slope of the linear motion equation. When combined with the zero offset, the system can accurately output the physical coordinates of the shedder.

An advantage of this tracking software is the availability of real-time tracking information. The user interface contains both a graph view and a spreadsheet view that displays the shedder position versus time. As the software records, it updates both of these displays immediately, so that trends can be identified immediately during testing. After the recording, this data can be exported to other data analysis software, like Microsoft Excel, in the .csv format.

3.5 Physical Testing

3.5.1 Procedure

The testing procedure used to collect the physical data was performed as follows

- Fix shedder to oscillator
- Initiate flow at a constant velocity of 0.18 m/s
- Adjust hanging mass to vary natural frequency
- Record oscillator motion using tracking software

This procedure was performed for a series of hanging masses. The first mass recorded was 25 grams, the second mass was 50 grams, and the mass was increased by 50 grams until 800 grams was met.

The shedding frequency was calculated for each shape using the equation 19. St, Strouhal number, varies for each shape and was determined using CFD.

$$F_s = \frac{St \times U}{L} \quad \textbf{Equation 19}$$

Knowing the expected shedding frequency, the damped natural frequency of the shedder-oscillator could be modified to match it. Using the closed-form solution for the un-damped natural frequency of the shedder-oscillator, a starting point for the frequency tuning was established:

$$W_n = \sqrt{\frac{W}{mL}} \quad \textbf{Equation 20}$$

Where W is the weight that is hung from the thread, m is the mass of the shedder-oscillator system (not including the hanging mass), and L is the thread length, measured from the point of attachment on the shedder-oscillator beam to the center of the pulley. The natural frequency varies while the shedding frequency remains the same.

5. Experimental Results

Physical testing provided a comprehensive look into the behavior of the various shedder geometries at a consistent flow condition. Several different types of analyses were performed on the raw data in order to determine different behavior characteristics. Each of these characteristics allows different conclusions to be drawn, thereby providing a broad comparison of the shedder geometries. These conclusions are defined as Identification of Lock-In, Physical Oscillation Amplitude, and Power Conversion.

5.1 Identification of Lock-In

The identification of the lock-in condition was a primary goal of physical testing. Previous research has shown that matching the natural frequency of the oscillator to the shedding frequency produces the largest physical amplitudes due to resonance. In order to determine if and under what conditions each of the geometries operates in lock-in, a data analysis technique was developed to quantify the oscillation regularity and frequency. This technique utilizes the Fast Fourier Transform to determine the dominant frequency and non-dimensional amplitude associated with each natural frequency step.

5.1.1Analysis Procedure

5.1.1.1Raw Data

The data analysis procedure started with the raw data produced by the optical tracking system. This data was in the .CSV (comma separated values) file format, and consisted of two columns: the time instant the position was recorded in seconds and the position in inches from the calibrated zero point. Each trial consists of approximately 200 seconds of position data.

5.1.1.2 Raw Data Normalization

Since the optical tracking system only records time and position data when movement has been detected, the sampling rate varied throughout the data. It was important to eliminate these variations in order to perform an accurate Fast Fourier Transform calculation on the data. This was accomplished by determining an equal time step (Equation 21), based on the number of desired data points and the total time of data recording.

$$t_{equal\ step} = \frac{t_{total}}{4096} \quad \textbf{Equation 21}$$

For each trial, the data was normalized to 4096 data points, in order to be acceptable to the Fast Fourier Transform process, which requires the number of data points to be of the form 2^n (2, 4, 8, 16, 32, etc.). The number 4096 was chosen because the number of data points recorded in each trial run is closer to 4096 than any other power of 2.

With a series of equal time steps, the data was then fit to the equal time steps using a closest match function. The match function looked at each equal time step, determined the closest match to a time step, and inserted the position for that time step. The result was position vs. time data that was equally spaced and ready for FFT analysis.

5.1.1.3 FFT Calculation

This normalized data was inserted into a Microsoft Excel template, which contained functions and macros to calculate the FFT and report the results of interest. The FFT was calculated from the normalized position data using the "Fourier Analysis" macro included as part of the Analysis Add-In. The complex results of the FFT were plotted in a separate column. The real FFT amplitude was calculated based on these complex results according to the formula:

$$FFT\ Amplitude = \frac{2}{4096} \times IMABS(FFT\ Result) \quad \textbf{Equation 22}$$

where the IMABS() function returns the absolute value (modulus) of a complex number.

The FFT frequency step was calculated according to the following formula:

$$f_{step} = \frac{f_{sampling}}{4096} \quad \textbf{Equation 23}$$

Where

$$f_{sampling} = \frac{4096}{t_{total}} \quad \textbf{Equation 24}$$

The spreadsheet then determines the maximum FFT amplitude, and returns it along with the associated frequency. These results are recorded separately for each of the 17 runs, over 3 trials, for 4 shedder geometries, resulting in 204 pairs of FFT amplitudes and dominant frequencies.

5.1.2 Summary of FFT Amplitude Results

For each mass increment, the FFT amplitudes and dominant frequencies were averaged over the three trials. In order to compare the shedder geometries, these computed oscillation frequencies were normalized to the shedding frequency of the shedder at the given flow condition.

Using the Strouhal number from computational fluid dynamics for the shedder, the test flow velocity, and the characteristic length, the shedding frequency was calculated.

$$f_s = \frac{St \times U}{L} \quad \textbf{Equation 25}$$

The characteristic length for the cylinder was taken to be equivalent to the diameter, while the length of the tail was taken for each of the T shapes. The oscillator natural frequency varies with the hanging mass, and is calculated according to:

$$f_n = \sqrt{\frac{k}{m}} = \sqrt{\frac{m_h g}{m_b L}} \div 2\pi$$ **Equation 26**

where

$m_h = Hanging\ Mass\ [kg]$

$m_b = Beam\ Mass\ (including\ shedder)\ [kg]$

$L = Length\ of\ String\ [m]$

Cylinder

Table 1 - FFT Results for the cylinder shedder

Cylinder Data

	Trial A		Trial B		Trial C			
Mass	FFT Amp	Frequency	FFT Amp	Frequency	FFT Amp	Frequency	Avg. FFT Amp.	Avg. Frequency
25	0.046	0.047	0.108	0.014	0.064	0.060	0.073	0.040
50	0.031	0.089	0.046	0.050	0.035	0.022	0.037	0.054
100	0.020	0.052	0.033	0.011	0.023	0.069	0.025	0.044
150	0.014	0.047	0.026	0.443	0.036	0.904	0.026	0.465
200	0.032	0.909	0.033	0.780	0.068	1.093	0.044	0.927
250	0.017	0.987	0.034	0.845	0.088	1.181	0.046	1.004
300	0.018	1.112	0.017	0.860	0.063	1.234	0.033	1.069
350	0.012	1.070	0.021	0.867	0.073	1.288	0.036	1.075
400	0.016	1.096	0.019	1.002	0.056	1.428	0.031	1.175
450	0.019	1.143	0.020	1.042	0.036	1.474	0.025	1.219
500	0.016	1.171	0.017	1.070	0.012	1.612	0.015	1.284
550	0.013	1.207	0.014	1.201	0.006	1.529	0.011	1.312
600	0.015	1.200	0.011	1.168	0.004	1.575	0.010	1.314
650	0.012	1.227	0.009	1.191	0.003	0.259	0.008	0.892
700	0.007	1.417	0.008	1.111	0.003	0.150	0.006	0.893
750	0.009	1.244	0.007	1.217	0.004	0.205	0.007	0.889
800	0.005	1.370	0.004	1.097	0.003	0.092	0.004	0.853

$$f_s = \frac{St \times U}{L} = \frac{0.19 \times 0.17}{0.03175} = 1.02\ Hz$$

In this case the mass of the beam was taken to be 0.481 kg, and the length of the string 5.25 in = 0.133 m.

The following plots show the FFT amplitude and dominant frequency plotted against normalized frequency.

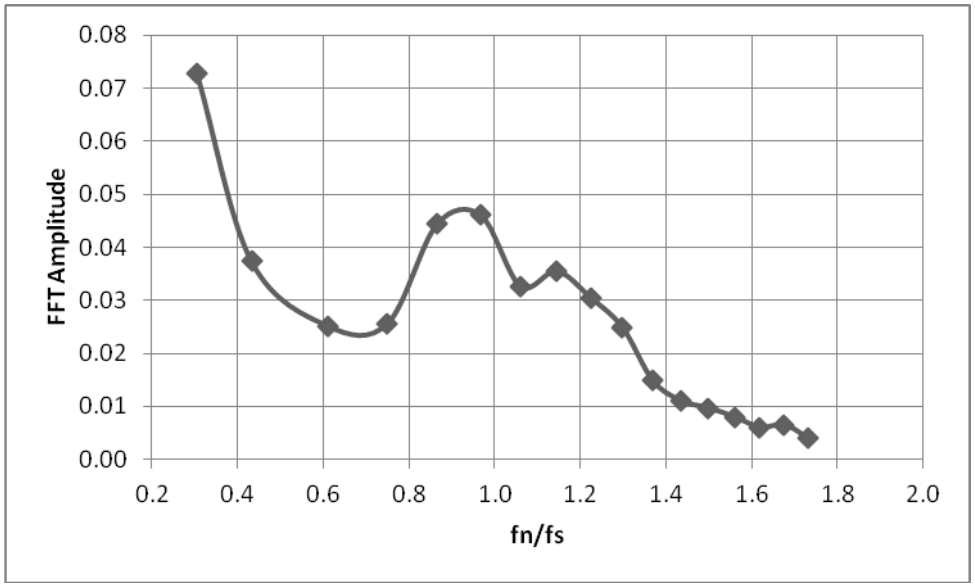

Figure 26 - FFT Amplitude vs. normalized natural frequency for the cylinder shedder.

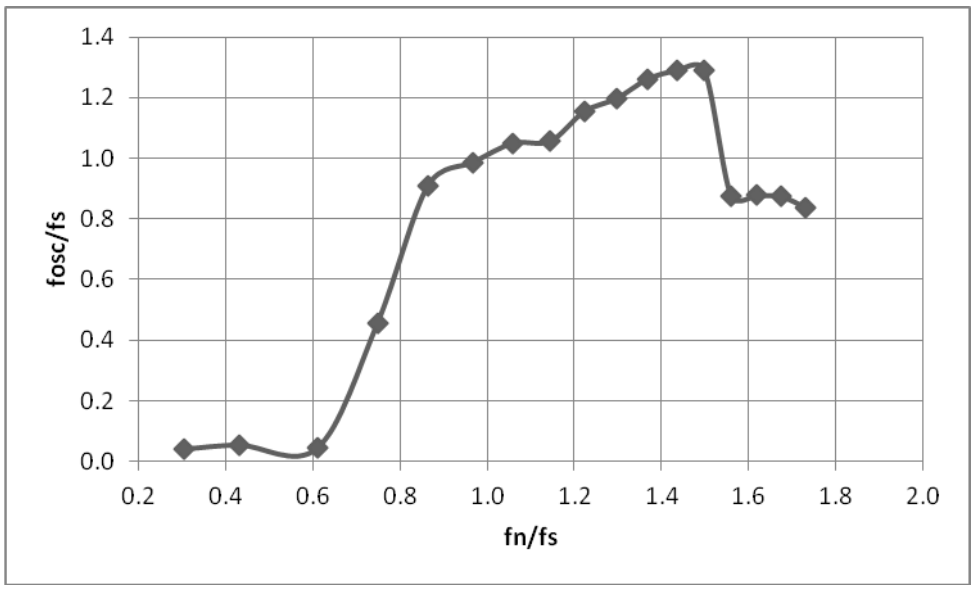

Figure 27 - Normalized oscillation frequency vs. normalized natural frequency for the cylinder shedder.

This curves show how the amplitudes and frequencies vary as the system moves towards and away from the lock-in condition. What we see is a peak in amplitude near the resonance point. The high FFT amplitude at the low range of frequency ratio is the result of low (almost zero) oscillation frequency. From the frequency plot, it can be seen that the cylinder started oscillating periodically when the natural frequency was between about 80% and 150% of the shedding frequency.

Curved 1:1.5 T

Table 2 - FFT Results for the Curved 1:1.5 T shedder.

Curved T 1:1.5

	Trial A		Trial B		Trial C			
Mass	FFT Amp	Frequenc	FFT	Frequenc	FFT	Frequenc	Avg. FFT	Avg.
25	0.260	0.214	0.351	0.237	0.255	0.206	0.289	0.219
50	0.277	0.332	0.282	0.352	0.179	0.352	0.246	0.345
100	0.213	0.479	0.237	0.521	0.149	0.527	0.199	0.509
150	0.174	0.599	0.176	0.585	0.121	0.546	0.157	0.577
200	0.088	0.620	0.101	0.635	0.087	0.699	0.092	0.651
250	0.079	0.717	0.099	0.719	0.061	0.685	0.080	0.707
300	0.051	0.833	0.065	0.831	0.042	0.733	0.052	0.799
350	0.032	0.843	0.049	0.754	0.031	0.921	0.037	0.839
400	0.018	0.725	0.036	0.948	0.024	0.854	0.026	0.842
450	0.012	1.111	0.024	0.931	0.022	0.959	0.019	1.000
500	0.009	0.535	0.014	1.099	0.012	0.778	0.011	0.804
550	0.007	0.900	0.011	0.909	0.011	0.681	0.010	0.830
600	0.007	0.029	0.009	0.684	0.008	0.952	0.008	0.555
650	0.007	0.022	0.007	0.751	0.007	0.094	0.007	0.289
700	0.006	0.014	0.006	0.493	0.007	0.056	0.006	0.188
750	0.005	0.043	0.005	0.628	0.004	0.052	0.004	0.241
800	0.003	0.047	0.005	0.031	0.005	0.030	0.004	0.036

$$f_s = \frac{St \times U}{L} = \frac{0.10 \times 0.17}{0.0381} = 0.446\ Hz$$

In this case the mass of the beam was taken to be 0.411 kg, and the length of the string 5.25 in = 0.133 m.

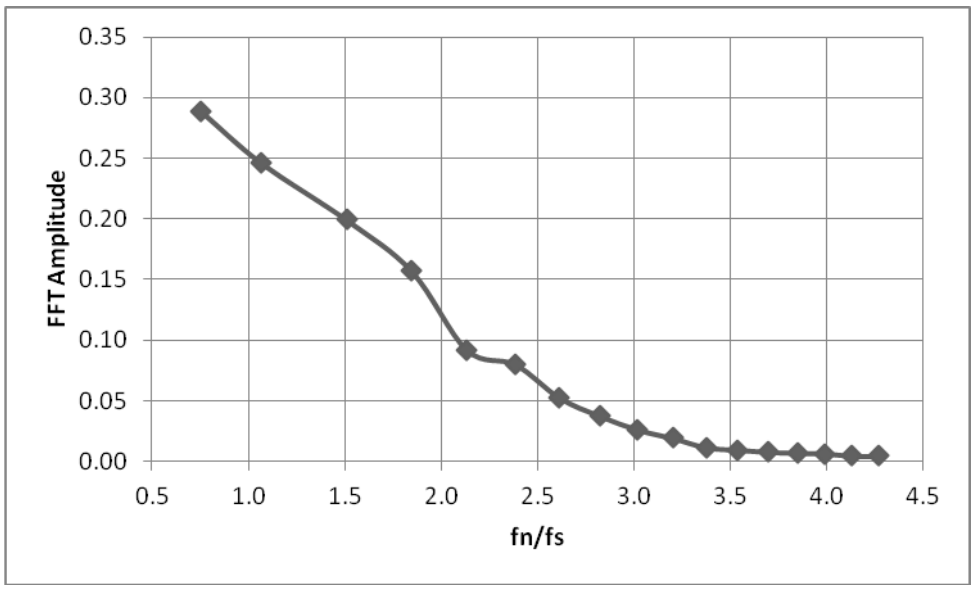

Figure 28 - FFT Amplitude vs. normalized natural frequency for the curved T shedder.

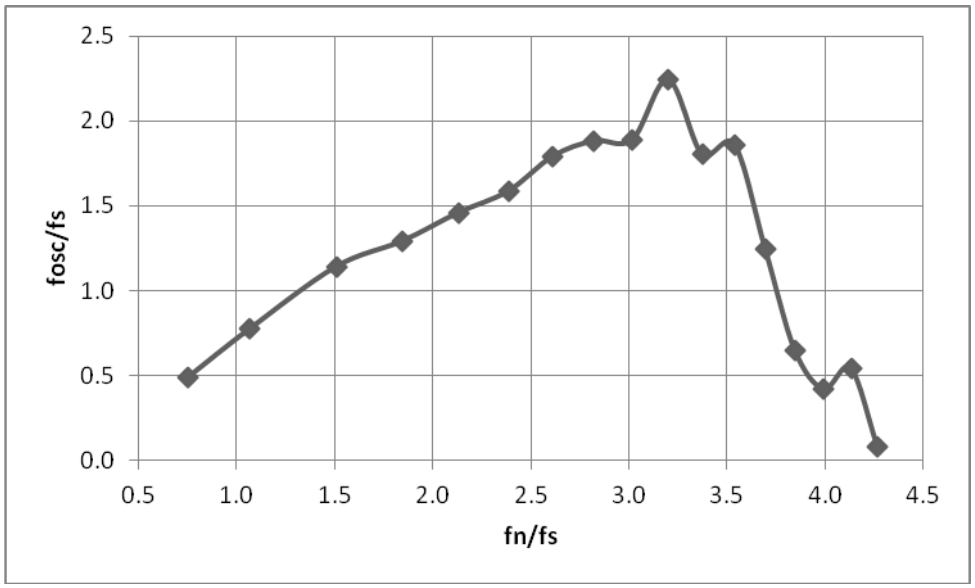

Figure 29 - Normalized oscillation frequency vs. normalized natural frequency for the curved T shedder.

The amplitude plot for the curved T shedder shows no definite peak, but does exhibit a consistent drop in amplitude as the natural frequency moves further away from the shedding frequency. From the frequency plot, we can see that the shedder oscillated periodically until the natural frequency was 350% of the shedding frequency. This is a much larger frequency range than the cylinder.

Straight 1:1.5 T

Table 3 - FFT Data for Straight 1:1.5 T

Straight T 1:1.5

	Trial B		Trial C		Trial D			
Mass	FFT Amp	Frequenc	FFT	Frequenc	FFT	Frequenc	Avg. FFT	Avg.
25	0.355	0.225	0.430	0.264	0.308	0.228	0.364	0.239
50	0.416	0.355	0.371	0.402	0.410	0.380	0.399	0.379
100	0.270	0.522	0.253	0.541	0.294	0.522	0.272	0.528
150	0.154	0.597	0.198	0.683	0.186	0.654	0.179	0.645
200	0.091	0.659	0.129	0.722	0.182	0.693	0.134	0.691
250	0.063	0.764	0.110	0.769	0.113	0.763	0.095	0.765
300	0.075	0.782	0.075	0.840	0.080	0.799	0.077	0.807
350	0.129	0.891	0.058	0.854	0.051	0.808	0.079	0.851
400	0.044	0.970	0.044	0.947	0.031	0.879	0.040	0.932
450	0.042	1.031	0.028	0.872	0.014	0.738	0.028	0.880
500	0.029	0.981	0.029	0.886	0.011	0.944	0.023	0.937
550	0.026	1.004	0.019	1.048	0.006	0.025	0.017	0.692
600	0.020	1.018	0.013	0.755	0.006	0.068	0.013	0.614
650	0.012	1.092	0.012	0.728	0.006	0.073	0.010	0.631
700	0.011	1.100	0.008	0.714	0.006	0.035	0.008	0.616
750	0.006	1.130	0.007	0.982	0.004	0.018	0.006	0.710
800	0.007	0.713	0.005	0.795	0.006	0.034	0.006	0.514

$$f_s = \frac{St \times U}{L} = \frac{0.10 \times 0.17}{0.0381} = 0.446\ Hz$$

In this case the mass of the beam was taken to be 0.411 kg, and the length of the string 5.25 in = 0.133 m.

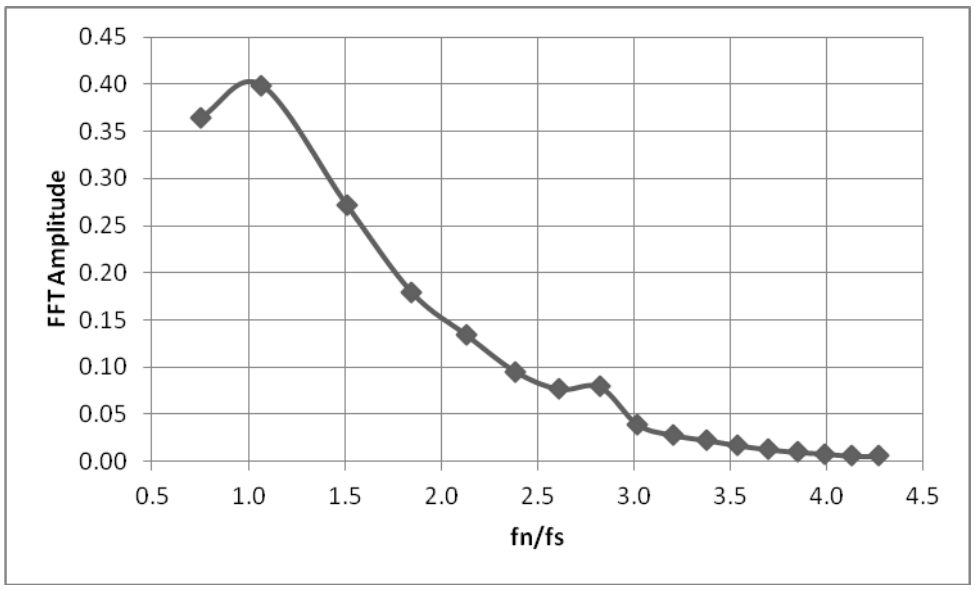

Figure 30 - FFT Amplitude vs. normalized natural frequency for the straight 1:1.5 T shedder.

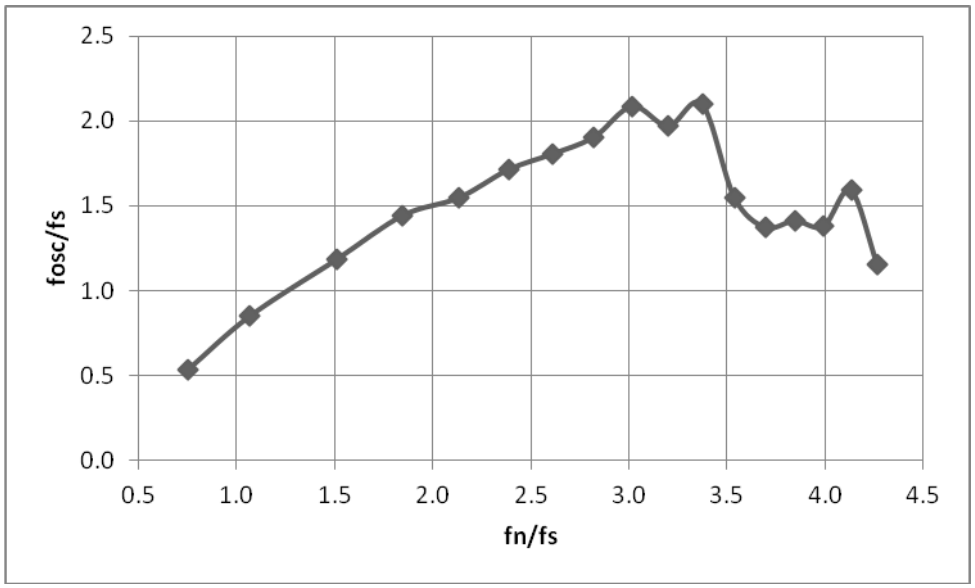

Figure 31 - Normalized oscillation frequency vs. normalized natural frequency for the straight 1:1.5 T shedder.

The amplitude plot for the straight 1:1.5 T shedder shows a definite peak in amplitude at the resonance point. The 1:1.5 T shedder oscillated periodically for natural frequencies up to about 350%, similar to the curved T shedder.

Straight 1:1 T

Table 4 - FFT data for the Straight 1:1 T shedder.

Straight T 1:1

	Trial A		Trial B		Trial C			
Mass	FFT Amp	Frequenc	FFT	Frequenc	FFT	Frequenc	Avg. FFT	Avg.
25	0.498	0.321	0.581	0.328	0.291	0.313	0.395	0.317
50	0.380	0.461	0.350	0.450	0.473	0.451	0.427	0.456
100	0.199	0.612	0.309	0.607	0.286	0.616	0.243	0.614
150	0.139	0.818	0.160	0.789	0.179	0.783	0.159	0.800
200	0.101	0.868	0.140	0.889	0.117	0.904	0.109	0.886
250	0.081	0.964	0.120	0.993	0.072	0.867	0.077	0.915
300	0.033	1.110	0.081	1.105	0.060	1.043	0.046	1.076
350	0.023	1.080	0.070	1.130	0.034	1.038	0.028	1.059
400	0.013	1.120	0.017	1.270	0.013	0.983	0.013	1.052
450	0.012	1.320	0.009	1.440	0.007	1.015	0.010	1.167
500	0.008	1.230	0.009	0.079	0.007	0.044	0.007	0.637
550	0.009	0.034	0.006	0.080	0.009	0.013	0.009	0.024
600	0.006	0.090	0.007	0.025	0.004	0.023	0.005	0.056
650	0.005	0.023	0.006	0.049	0.005	0.022	0.005	0.023
700	0.007	0.038	0.007	0.014	0.006	0.013	0.006	0.025
750	0.005	0.020	0.008	0.020	0.004	0.044	0.004	0.032

$$f_s = \frac{St \times U}{L} = \frac{0.10 \times 0.17}{0.0254} = 0.669\ Hz$$

In this case the mass of the beam was taken to be 0.401 kg, and the length of the string 5.25 in = 0.133 m.

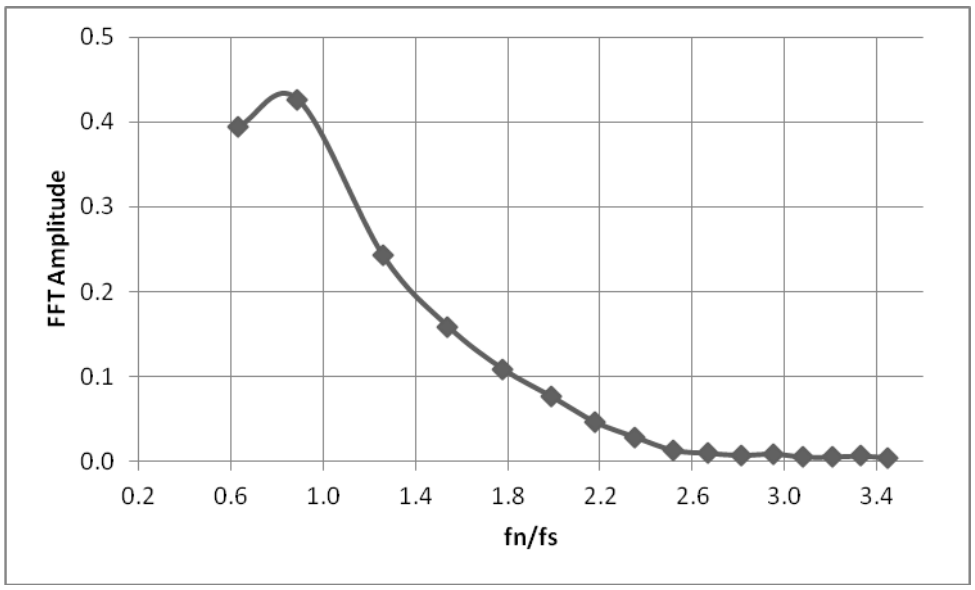

Figure 32 - FFT Amplitude vs. normalized natural frequency for the straight 1:1 T shedder.

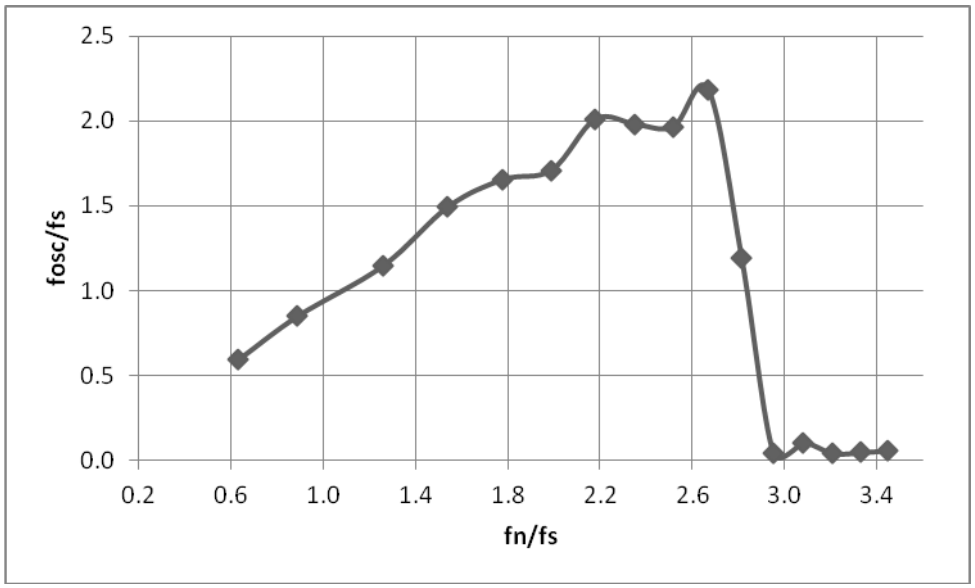

Figure 33 - Normalized oscillation frequency vs. normalized natural frequency for the straight 1:1 T shedder.

The 1:1 T shedder exhibited the smoothest amplitude curve with a definite peak near the resonant point. The frequency plot shows periodic oscillation for natural frequencies up to about 260% of the shedding frequency. This is a smaller range of oscillation than either the curved T or the 1:1.5 straight T shedder.

Geometry Comparison

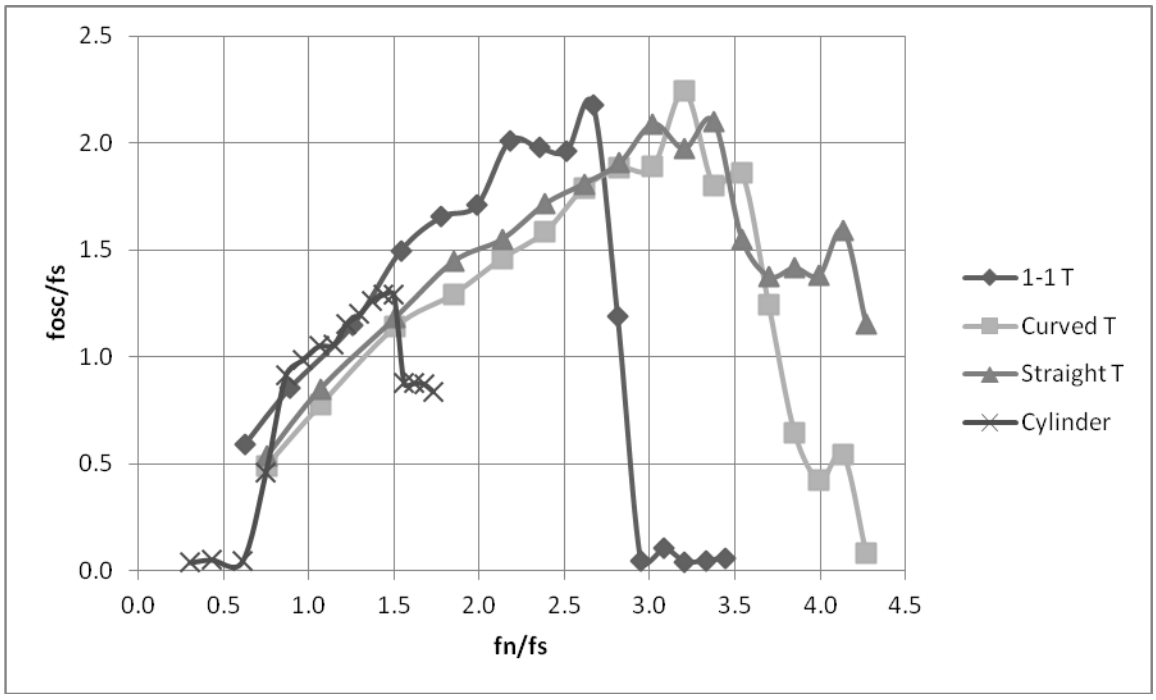

Figure 34 - Normalized oscillation frequency vs. normalized natural frequency for the each of the shedder geometries.

Figure 31 shows the ranges of oscillation for each of the four shedder geometries. It is evident that the cylinder had the smallest oscillation range, followed by the 1:1 T, then the curved and 1:1.5 T shedders (which have comparable drop-off points).

5.2Physical Amplitude and Frequency

In addition to the non-dimensional FFT amplitudes, it was important to consider the shedder geometries that resulted in the greatest physical oscillation amplitude.

5.2.1RMS Amplitude Calculation

This was calculated using the root mean square (RMS) method:

$$RMS\ Amplitude = \sqrt{mean(x_{1\to n}^2)}$$ **Equation 27**

Summary of RMS Amplitude Results

Table 5 - RMS Amplitudes for each of the four shedder geometries.

RMS Amplitudes [in]

	A	B	C	Average
Cylinder	0.17	0.18	0.29	0.21
Curved T	0.57	0.56	0.45	0.53
1:1.5 Str. T	0.70	0.72	0.73	0.71
1:1 Str. T	0.80	0.82	0.76	0.79

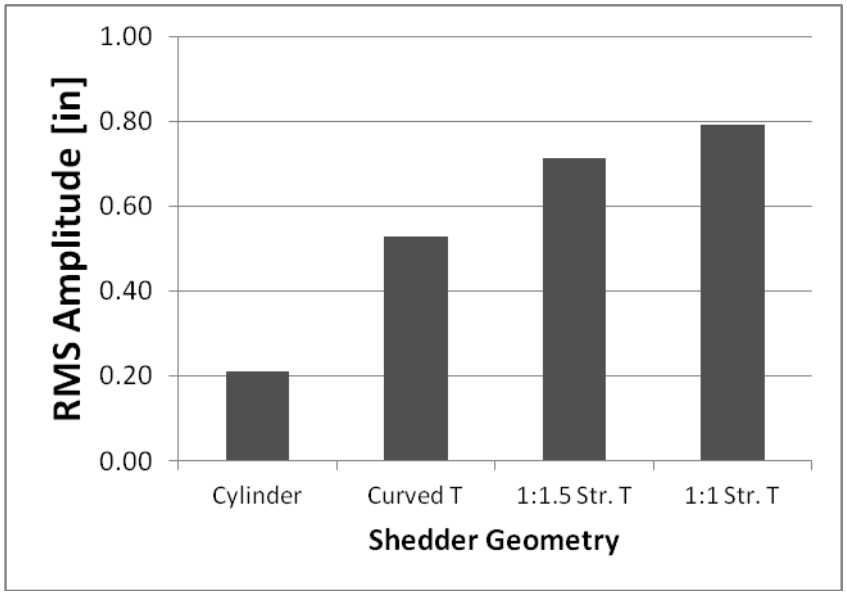

Figure 35 - Graph comparing the RMS physical amplitudes for each of the four shedder geometries.

These results show that the 1:1 Straight T exhibited the highest oscillation amplitude of the four geometries.

5.2.2Summary of Frequency Results

In addition to the physical amplitudes, the oscillation frequency was also recorded at the lock-in condition for each of the geometries.

Table 6 - Summary of FFT frequencies at lock-in for each of the shedder geometries.

Frequencies [Hz]

	A	B	C	Average
Cylinder	0.91	0.84	1.18	0.98
Curved T	0.33	0.35	0.35	0.35
1:1.5 Str. T	0.35	0.40	0.38	0.38
1:1 Str. T	0.32	0.33	0.31	0.32

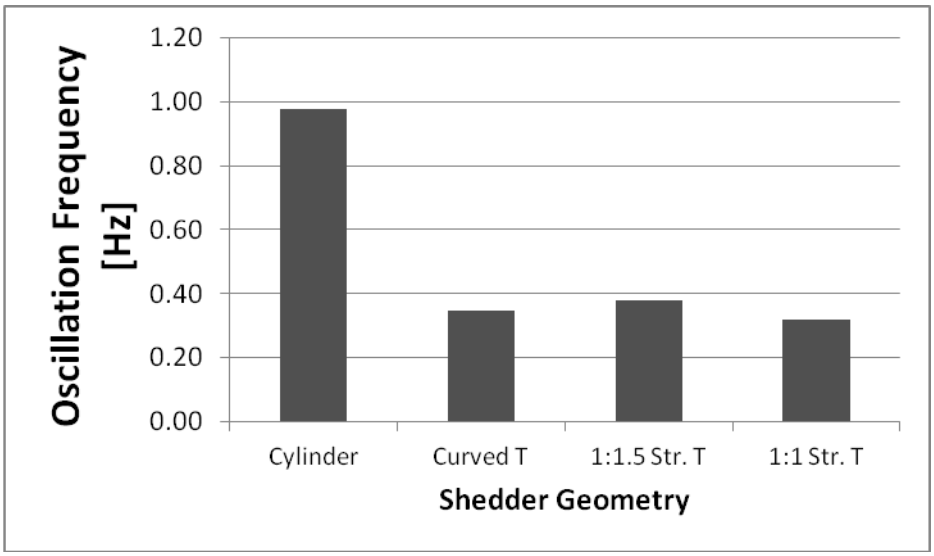

Figure 36 - Graph comparing the oscillation frequencies at lock-in for each of the four shedder geometries.

5.3 Power

In addition to the shedder oscillation characteristics such as regularity, frequency, and RMS amplitude, it is important to quantify the energy conversion ratio for each of the geometries. Since the end use for any of these geometries is to be used as the driver for a power extraction system, it is critical to look at how much of the flow energy is converted to mechanical energy.

The power results presented here are total mechanical energy in the system. The amount of extracted power will depend on the attached power generation system (high damping). These results do however, quantify the maximum power available to be extracted by such a system and are still an accurate measure of energy conversion.

5.3.1Power equation description

The equation used to calculate RMS power values is based on the mechanical energy of the oscillator system, including the potential energy of the hanging mass, and the kinetic energy of the moving shedder.

$$E = \frac{1}{2}kx^2 + \frac{1}{2}mv^2 \quad \textbf{Equation 28}$$

$$P = \dot{E} = kx\dot{x} + m\dot{x}\ddot{x} \quad \textbf{Equation 29}$$

5.3.2Numerical Power calculation from raw data

To ensure accurate calculations, power was calculated numerically based on the raw data from each oscillation trial. The x value is the position data value, while $\dot{x}$ is calculated as a change in position divided by the change in time:

$$\dot{x} = \frac{(x_2 - x_1)}{(t_2 - t_1)} \quad \textbf{Equation 30}$$

The acceleration term $\ddot{x}$ was similarly calculated from the velocity terms above:

$$\bar{x} = \frac{(\dot{x}_2 - \dot{x}_1)}{(t_2 - t_1)}$$ **Equation 31**

The resulting data was an oscillating power value. In order to quantify it to a single value, the RMS method outlined previously was used.

Summary of Power results

RMS Power					
	A	B	C	Avg. RMS Power [W]	Standard Dev. [W]
Cylinder	21	37	149	69	57
Curved T	36	58	244	113	93
1:1.5 Str. T	165	288	0	151	118
1:1 Str. T	187	479	138	268	151

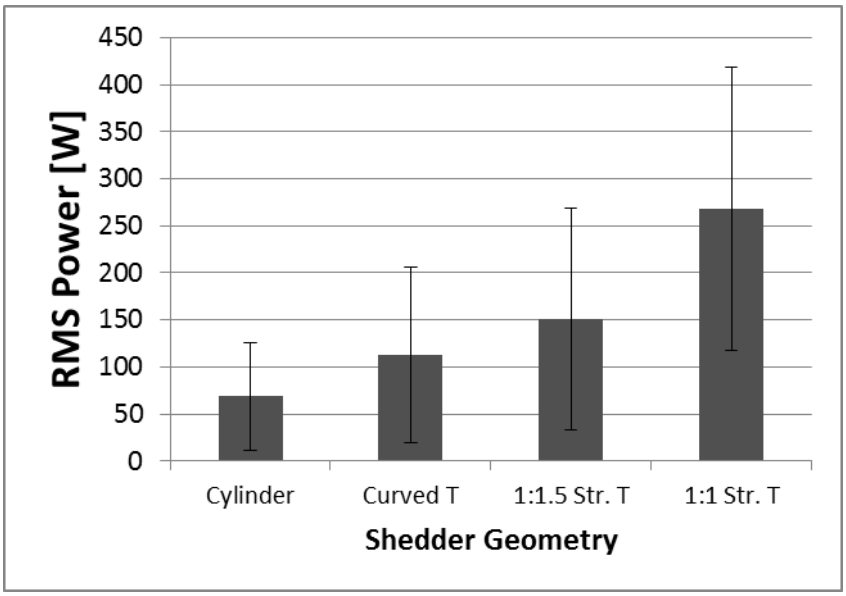

Figure 37 - RMS Power in the oscillator system with 1 standard deviation error bars.

While the data shows a significant trend, there is large variation between trials for each of the shedder geometries. The large discrepancies are due to the fact that the power was calculated numerically from the raw time domain data. Each trial contained a certain number of outliers that affected the resulting RMS Power values. Despite the influence of these outliers, the trend across

shapes is still accurate. The results from this calculation clearly show that the 1:1 Straight T geometry has the highest power conversion rate of the four tested geometries.

Based on these results, the 1:1 Straight T shedder geometry should be researched further and considered when designing a future power extraction system.

6. Conclusion and Discussion

Based on the collected data and its subsequent analysis, several conclusions can be drawn about the oscillation behavior of each of the shedder geometries.

6.1 FFT Amplitude

Each of the shedder geometries had slightly different FFT amplitude curve shapes, but they all displayed the same trends. In each case (with the exception of the curved T), each shedder exhibited a distinguishable peak in amplitude near the point of frequency synchronization. Upon departing from the point of frequency synchronization, the FFT amplitude decreased significantly, indicating the shedder had smaller physical oscillation amplitudes. The geometry comparison plot also shows at what frequency the shedder oscillated as the natural frequency was adjusted away from the shedding frequency. The plots show a distinguishable range in which the shedder oscillated close to the shedding frequency. At the high end and low end, the frequencies tended to zero as the shedder did not move periodically. Practically, this is an important measure when considering real-world application conditions. A larger range of acceptable difference between the shedding frequency and natural frequency would allow a power generation system to operate at lock-in despite variations in flow velocity.

6.2 Identification of Lock-In

Based on the results of the FFT analysis, it can be concluded that the lock-in condition results in the highest oscillation regularity as defined by the FFT amplitude. For each of the four geometries, the oscillation regularity at the expected lock-in location was a local maximum.

6.3 RMS Amplitude and Frequency

The physical amplitudes and frequencies provide information about the oscillations in real terms. It is evident from the data that the cylinder oscillated at a much higher frequency than any of the T shapes. This is consistent with the conclusions drawn from the computational fluid dynamics analysis, which showed that the Strouhal number for the cylinder was approximately twice that of each of the T shapes.

When considering the physical amplitudes of the various shapes, it can be seen that the shedder geometry with the highest amplitude was the 1:1 T, followed by the straight T then the curved T and finally the cylinder. While the T shapes can all be directly compared because of their similarity in mass, the cylinder physical amplitude result must be considered with the fact that its mass was slightly higher than the T shapes. Regardless, the results show that each of the T shape shedders had a much higher physical oscillation amplitude.

6.4 Power/Energy

The experimental power results were also supported with theoretical calculations. The total energy stored in the system at any instant was the sum of the spring potential energy and the kinetic energy:

$$E = \frac{1}{2}kx^2 + \frac{1}{2}mv^2 \qquad \textbf{Equation 32}$$

This could be reduced to the following equation by using the amplitude, A, for the displacement, in which case the velocity was zero.

$$E = \frac{1}{2}kA^2$$ **Equation 33**

Using the relation that the maximum lift force, L=kA and that shedding frequency equals natural frequency (at lock-in) ω = sqrt(k/m), the stored energy became

$$E = \frac{1}{2}\frac{L^2}{m\omega^2}$$ **Equation 34**

This shows that the stored energy in the system increases with lift and decreases with shedder mass and shedding frequency. The shedder shape that exhibited the highest lift while having the lowest mass and shedding frequency was the 1:1 Straight T.

6.5 Recommendations

For future research, it is recommended that a more comprehensive list of geometries be tested. While the four geometries tested in this project represented simple cylinders and various T shapes, other geometries including variations in the T shape (like aspect ratio) may perform better than the 1:1 T shape, in terms of theoretical power output.

It is also recommended that in addition to geometry variation, there be some degree of optimization of the shape. This was found to be beyond the limits of the SolidWorks Flow Simulation's capabilities, or the researchers' skills at least.

In addition to continuing research into additional shedder geometries with computational fluid dynamics, the experimental testing should be improved by reconsidering the design of the flow tank and oscillator system. While each of these components worked well enough to obtain

conclusive results, many limitations and inefficiencies could be reduced or eliminated by further design considerations. Notably, the test section could be improved by redesigning the flow system to provide a more uniform flow profile. One design that was considered later on was an elevated open channel platform that would be attached to a reservoir on one side and open for the flow to exit on the other. The open channel platform would be hinged at the reservoir side, allowing the channel's angle of tilt to be increased or decreased depending on desired flow velocity in the channel. The reservoir would be filled with water via direct pumping until it reached the level of the attached open channel. Water would then be directed down the channel at a constant velocity, with uniform flow across the profile, and exit the other side in a waterfall-like fashion. The oscillator could also be designed to be more accurately counterbalanced to prevent undue stresses on the pivot joint. Friction should be reduced in this joint as much as possible in order to prevent friction losses that inhibit oscillations with small restoring forces.

Another area that could be explored is oscillator surface roughness and its effect on the generated vortices. It is known that at high Reynolds numbers, smooth surfaces expedite flow separation which would cause vortices to form closer to the body and therefore apply a stronger force on the body itself. This phenomenon can be further studied at low speed flow in an attempt to vary the shedder's surface roughness to optimize the lift force generated on the oscillator by the shedding vortices.

7.References

[1] Munson B., Young D., Okiihi T., and Huebsch W., 2009, *Fundamentals of Fluid Mechanics*, Wiley

[2] Techet, A., 2005, "Vortex Induced Vibrations I: Viscous Forces", *Design Principles for Ocean Vehicles (13.42),* MIT OpenCourseWare, Massachusetts Institute of Technology.

[3] Garcia E.M.H., 2008, "Prediction by Energy Phenomenology for Harnessing Hydrokinetic Energy Using Vortex-Induced Vibrations", Dissertation for P.h.D, University of Michigan.

[4] Blevins, R., 1990. "Flow-Induced Vibration" New York: Van Nostrand Reinhold.

[5] "Vortex Hydro Energy", n.d, from http://www.vortexhydroenergy.com/

[6] Bernitsas M., Raghavan K., Ben-Simon Y., Garcia E.M.H., 2008, "VIVACE (Vortex Induced Vibration Aquatic Clean Energy): A New Concept in Generation of Clean and Renewable Energy From Fluid Flow", Journal of Offshore Mechanics and Arctic Engineering, 130.

[7] Bernitsas M., Ben-Simon Y., Raghavan K., Garcia E.M.H., 2009, "The VIVACE Converter: Model Tests at high Damping and Reynolds Number Around 10^5", Journal of Offshore Mechanics and Arctic Engineering, 131.

[8] ISO International Standardization Organization, "Measurement of liquid flow in closed conduits - Weighing method", ISO 4185, 1980.

[9] W. Pöschel and R. Engel, "The concept of a new primary standard for liquid flow measurement at PTB Braunschweig," *Proceedings of the 9th International Conference on Flow Measurement (1998)*, pp. 1.

[10] Hall-Stinson A., Lehrman C., Tripp E., 2011,"Energy Generation From Vortex Induced Vibrations", MQP, Worcester Polytechnic Institute.

[11] Distler D., Johnson B., Kielbasa M., Phinney, B., 2011, “Optimization of Oscillating Body for Vortex Induced Vibrations”, MQP, Worcester Polytechnic Institute.

[12] White, F., 2011, “Fluid Mechanics 7e,” McGraw Hill: New York, NY, Chap. 6

[13] Idelchik, I. E., 1994, “Handbook of Hydraulic Resistance 3e”, CRC Press: Boca Raton, FL, Chap 8. pp. 519-520.

[14] The Engineering Toolbox, “Hazen-Williams factor for some common piping materials,” nd., http://www.engineeringtoolbox.com/hazen-williams-coefficients-d_798.html

[15] Lee, J., 2010, “Hydrokinetic Power Harnessing Utilizing Vortex Induced Vibrations Through A Virtual C-K VIVACE Model”, *Dissertation for P.h.D, University of Michigan.*

[16] Mei, C. C., 2003, “Flow Visualization: Electrolytic Techniques,” http://web.mit.edu/fluids-modules/www/

[17] Bradshaw, P., Mehta, R., 2003, “Wide Angle Diffuser,” from

http://www-htgl.stanford.edu/bradshaw/tunnel/wadiffuser.html

[18] “The Diffuser,” n.d., from

http://www.ivorbittle.co.uk/Books/Fluids%20book/Chapter%208%20web%20docs/Chapter%208%20The%20diffuser.htm

[19] Noui-Mehidi, M.N., Wu J., and Sutalo I., 2004, “Velocity Distribution in an Asymmetric Diffuser with Perforated Plates,” 15th Australasian Fluid Mechanics Conference, The University of Sydney, Sydney, Australia.

[20] Lee, J., Lu, T., Sun, H. Miao, G., 2010, “A Novel Formula to Describe the Velocity Profile

of Free Jet Flow,” Archive of Applied Mechanics, **81**(3)

[21] Cushman-Roisin, B., 2010, *Environmental Fluid Mechanics*, John Wiley & Sons, Inc., New York, pp. 154-155, Chap. 9

[22] R2 Resource Consultants, Inc., 2008, "Estimates of Turbine Mortality For Salmonids and Non-Salmonid Fish at Proposed Enloe Hydroelectric Project," Enloe Hydroelectric Project FERC No. 12569

[23] Georgia Tech Research Corporation, 2011, "Assessment of Energy Production Potential from Tidal Streams in the United States," DE-FG36-08GO18174

[24] Bernitsas, Michael M., 2006, "Low Head, Vortex Induced Vibrations River Energy Converter", DE-FG36-05GO15162, Vortex Hydro Energy LLC, Ypsilanti, Michigan

[25] García, Marcelo H., "Experimental Infrastructure, Ven Te Chow Hydrosystems Laboratory," from http://vtchl.illinois.edu/facilities/experimental/infrastructure

[26] "Utah State University, Utah Water Research Laboratory," n.d. from http://uwrl.usu.edu/facilities/hydraulics/about/facilities.html

[27] "HRTF: Hydraulic Research and Testing Facility", n.d. from http://hrtf.ce.umanitoba.ca/facilities.html

[28] ALDEN, "Alden - Hooper Low Reynolds Number Facility," from http://www.aldenlab.com/Services/Hooper_Low_Reynolds_Number_Facility

[29] Armfield Engineering Teaching Equipment & Research Equipment, "Laboratory Flumes and Channels for Hydraulic Teaching/Research Studies", from http://www.discoverarmfield.co.uk/data/pdf_files/flumes.pdf

[30] College of Engineering, University of Michigan, “MHL - Facilities: Low Turbulence Water Channel,” from http://www.engin.umich.edu/dept/name/facilities/mhl/facilities/low_turbulence.html

[31] Walker, D. T., Lyzenga, D. R., Ericson, E. A., and Lund, D. E., (1996), "Radar Backscatter and Surface Roughness Measurements for Stationary Breaking Waves," Proceedings of the Royal Society - Mathematical, Physical and Engineering Sciences (Series A), 452(1952), 1953-1984.

8.1 Appendix A

g	32.2	ft/s^2
	386.4	in/s^2
Flow Velocity	0.8	m/s
	2.6	ft/s
	31.5	in/s
Exit Area Diameter	6.0	in
Exit Screen Porosity	0.5	
Exit Area	14.1	in^2
Volume Flow	445.3	in^3/s
	6,939	gph
Ideal Head	1.3	in
Pipe Dia	3.0	in
Pipe Vel	63.0	in/s
Entrance K	0.5	
Entrance HL	2.6	in
Elbow K	0.3	
Elbow HL	1.5	in
Diffuser K	0.3	
Diffuser HL	1.5	in
Perf Plate/Screen K	3.4	
Perf Plate/Screen HL	4.4	in
Total Pipe Length	60	in
Hazen-Williams roughness	150	
Vol flow	115.65	gal/m
hydraulic diameter	3	in
f	3.11	fth20/100 ft pipe
	0.16	ft H20
	1.86	in
Head Losses	11.9	in
Required Head	13.2	in
	1.1	ft

8.2 Appendix B

Basic Geometric Analysis

Hanging mass (kg)

$$m := \frac{0.45}{9.81} \cdot 2.5$$

0.1146788991

Cylinder Diameter (m)

$$Dout := 0.02$$

0.02

Cylinder Length (m)

$$Clength := Dout \cdot 8$$

0.16

Horizontal distance between shedder and pulley (m)

$$L := \frac{(.30 - Clength)}{2}$$

0.07000000000

Maximum Expected Displacement

$$yMax := L$$

0.07000000000

$$Tension := m \cdot 9.81$$

1.125000000

$$\theta := \arctan\left(\frac{y}{L}\right)$$

$$\arctan(14.28571429y)$$

$$RestoringForce := -Tension \cdot \sin(\theta)$$

$$-\frac{16.07142858y}{\sqrt{1+204.0816328y^2}}$$

Buoyancy Effects

Cylinder Volume (m^3)

$$CVol := evalf\left(\frac{\mathrm{Pi}}{4}\cdot Dout^2\cdot Clength\right)$$

$$0.00005026548246$$

Buoyancy Force (N)

$$Buoy := (998\cdot CVol\cdot 9.81) - (0.238057743\, Clength)$$

$$0.4540289353$$

Static Forces (N)

$$f := RestoringForce + Buoy$$

$$-\frac{16.07142858y}{\sqrt{1+204.0816328y^2}} + 0.4540289353$$

Net force on the shedder as a function of displacement, d(m), (N)

$$plot(\mathrm{f}, \mathrm{y} = -\mathrm{yMax}..\mathrm{yMax})$$

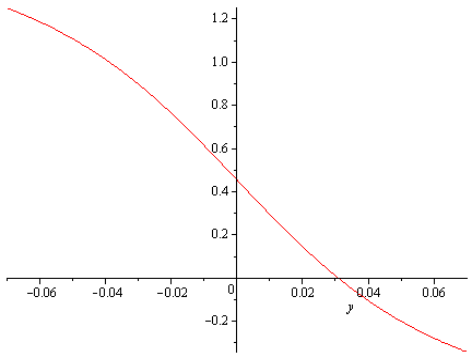

$NeutralPosition := solve(f = 0, y)$

$$0.03087696681$$

$with(Student[Precalculus]):$

Effective spring constant (N/m)

Exact Solution: diff(f, y), however a linear approximation is being made over the displacement range.

$k := \text{Slope}(f, -yMax, yMax)$

$$-11.36421613$$

Two "Springs" in Parallel, they add

$keff := 2\,k$

$$-22.72843226$$

Hypotenuse

$Hypot := \text{sqrt}(y^2 + L^2)$

$$\sqrt{y^2 + 0.004900000000}$$

Mass Displacement

$Dispm := Hypot - L$

$$\sqrt{y^2 + 0.004900000000} - 0.07000000000$$

Motion ratio d / Dism

$Ratio := \frac{Dispm}{y}$

$$\frac{\sqrt{y^2 + 0.004900000000} - 0.07000000000}{y}$$

Shedder and Hanging mass, (kg)

$msys := .250 + (Ratio \cdot m)$

$$0.250 + \frac{0.1146788991\left(\sqrt{y^2 + 0.004900000000} - 0.07000000000\right)}{y}$$

Natural Angular Frequency (rad/s)

$w := \text{sqrt}\left(\frac{\text{abs}(keff)}{msys}\right)$

$$4.767434557 \left(1 \Big/ \left(0.250 + \frac{0.1146788991\left(\sqrt{y^2 + 0.004900000000} - 0.07000000000\right)}{y}\right)\right)^{1/2}$$

$eval(w, y = -yMax)$

10.59433970

$eval(w, y = yMax)$

8.740577340

$$ApproxFn := \frac{(eval(w, y = -yMax) - eval(w, y = yMax))}{2} + eval(w, y = yMax)$$

9.667458520

Natural Freuqency (cycles/s)

$H := \frac{w}{2 \cdot \text{Pi}}$

$$\frac{1}{\pi}\left(2.383717278\left(1\Big/\left(0.250+\frac{0.1146788991\left(\sqrt{y^2+0.004900000000}-0.07000000000\right)}{y}\right)\right)^{1/2}\right)$$

$$ApproxFnHz := evalf\left(\frac{(eval(H, y=-yMax) - eval(H, y=yMax))}{2}\right) + evalf(eval(H, y=yMax))$$

$$1.538623809$$

Flow Calculations

Now Working Backwards to an ideal flow velocity (m/s):

$$Uideal := evalf\left(\frac{ApproxFn \cdot Dout}{0.198} + \frac{19.7 \cdot 1.31 \cdot 10^{-6}}{Dout}, 2\right)$$

$$0.97$$

$$MaxShedForce := 0.5 \cdot 998 \cdot 0.8^3 \cdot Dout \cdot Clength \cdot 0.6$$

$$0.490536960$$

$$NetForce := MaxShedForce + Buoy + RestoringForce$$

$$0.9445658953 - \frac{16.07142858y}{\sqrt{1 + 204.0816328y^2}}$$

$$top := solve(NetForce = 0, y)$$

$$0.1082010204$$

$$NetForce := -MaxShedForce + Buoy + RestoringForce$$

$$-0.0365080247 - \frac{16.07142858y}{\sqrt{1 + 204.0816328y^2}}$$

$$bottom := solve(NetForce = 0, y)$$

$$-0.002272807492$$

$$totalDisp := top - bottom$$

$$0.1104738279$$

Results

Total Displacement (cm):

$$evalf(totalDisp \cdot 100, 3)$$

$$11.0$$

Flow Velocity (m/s):

$$Uideal$$

$$0.97$$

Shedder Length (cm)

$$Clength \cdot 100$$

$$16.00$$

8.3 Appendix C

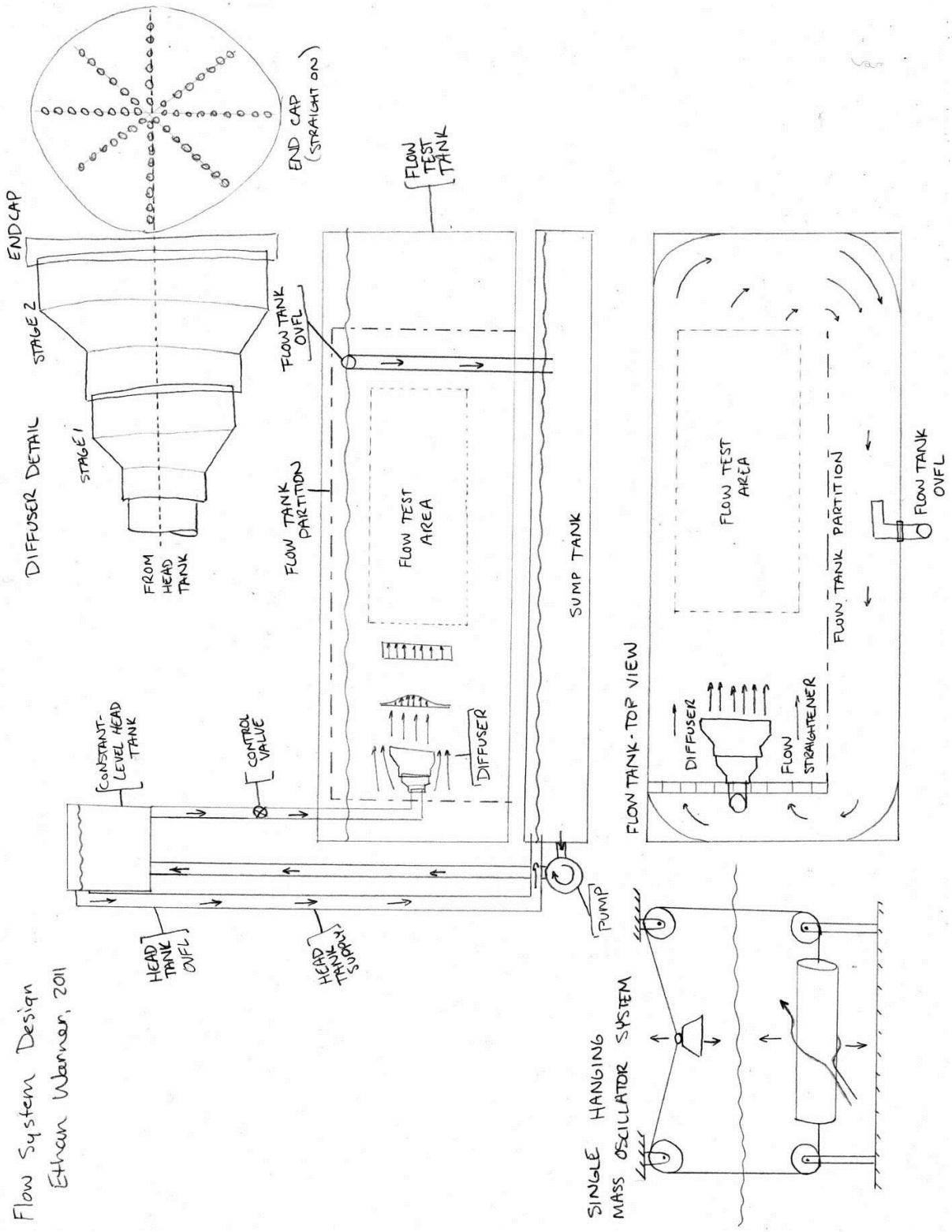

8.4 Appendix D

Solidworks Flow Simulation Input Parameters

External Flow

Mesh = 5

Global Goal

CFD Detailed Results

Cylinder	1 in.								
RE	Velocity	Force Amp	Freq	St	Cl (rms)		Computational Domain Limits:		
2000	0.078898	0.0019896	0.565914	0.182187	0.438775			0.12192	m
4000	0.157796	0.0076522	1.1473	0.184678	0.421882			0.08128	m
6000	0.236694	0.0166036	1.725639	0.185181	0.406843				
8000	0.315592	0.0294478	2.318968	0.186639	0.405881			Span:	
10000	0.39449	0.0453001	2.917752	0.187865	0.399599			0.04064	m
12000	0.473388	0.0640489	3.521378	0.188942	0.392351				
							Cylinder Diameter:		
								0.0254	m
1:1 T	.25 thick								
RE	Velocity	Force Amp	Freq	St	Cl (rms)		Computational Domain Limits:		
2000	0.063118	0.0024741	0.304101	0.122376	0.68202			0.12192	m
4000	0.126237	0.0097981	0.612701	0.123281	0.675241			0.08128	m
6000	0.189355	0.0222608	0.89709	0.120335	0.681827				
8000	0.252473	0.0391662	1.231614	0.123906	0.674788			Span:	
10000	0.315592	0.0538465	1.604003	0.129096	0.593736			0.04064	m
12000	0.37871	0.0776624	1.927624	0.129285	0.594681				
								T "chord":	
								0.03175	m
1:1.5 T	.25 thick								
RE	Velocity	Force Amp	Freq	St	Cl (rms)		Computational Domain Limits:		
2000	0.045085	0.0007	0.17334	0.097657	0.270148			0.12192	m
4000	0.090169	0.0025	0.353357	0.099538	0.241204			0.08128	m
6000	0.135254	0.00586	0.473934	0.089003	0.25128				
8000	0.180338	0.0107366	0.784929	0.110554	0.258969			Span:	
10000	0.225423	0.0159862	0.952381	0.107312	0.246779			0.04064	m
12000	0.270507	0.0221986	1.136364	0.106702	0.237972				
								T "chord":	
								0.04445	m

Curved T	.25 thick								
RE	Velocity	Force Amp	Freq	St	Cl (rms)		Computational Domain Limits:		
2000.05188	0.0526	0.0075997	0.201207	0.097161	0.402206			0.254	m
4000.10376	0.1052	0.0283516	0.423729	0.102307	0.375121			0	m
6000.15564	0.1578	0.0623	0.666667	0.107309	0.366353				
8000.20752	0.2104	0.0978	0.833333	0.100602	0.323499			Span:	
10000.2594	0.263	0.1492638	1.136364	0.109748	0.315987			0.254	m
12000.31128	0.3156	0.226831	1.136364	0.091456	0.333468				
								T "chord":	
								0.0381	m

8.4 Appendix E

Vernier Flow Rate Sensor Calibration Curve

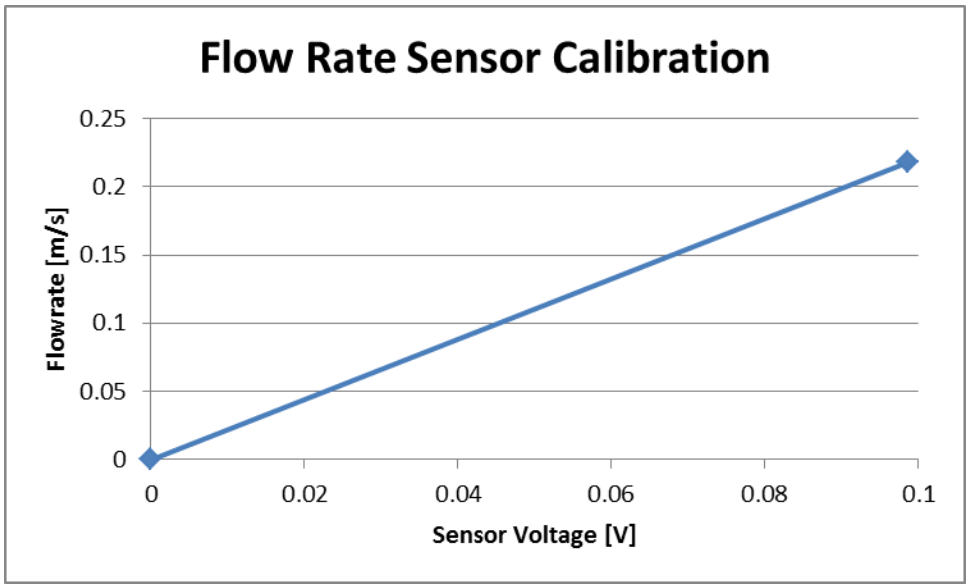

Figure 38 - Flow Rate Sensor Calibration Curve